# Helical core flow from geomagnetic secular variation

Hagay Amit*, Peter Olson

*Department of Earth and Planetary Sciences, Johns Hopkins University, Baltimore, MD 21218, USA*

## Abstract

Fluid flow below the core-mantle boundary is inferred from geomagnetic secular variation data, assuming frozen magnetic flux and a new physical assumption termed helical flow, in which the tangential divergence correlates with the radial vorticity. Helical flow introduces streamfunction diffusion and removes non-uniqueness in the inversion of the magnetic induction equation. We combine helical flow with tangential geostrophy and compare the following physical assumptions: tangential geostrophy, strong helicity, weak helicity and columnar flow, using geomagnetic field models from the 2000 Oersted and 1980 Magsat satellites. Our solutions contain some features found in previous core flow models, such as large mid-latitude vortices, westward drift in most of the southern hemisphere, and suggested polar vortices. However, our solutions contain significantly more flow along contours of the radial magnetic field than previous core flow models.
© 2004 Elsevier B.V. All rights reserved.

*Keywords:* Helical flow; Secular variation; Geomagnetic field; Core-mantle boundary; Frozen flux; Tangential geostrophy

## 1. Introduction

Mapping the flow in Earth's liquid outer core places constraints on the geodynamo, the thermal structure of the core, and the nature of core-mantle coupling. Geomagnetic data provided by the Danish Oersted satellite in 2000, combined with the data from the US Magsat satellite in 1980, give a global model of the Earth's magnetic field and its secular variation on the core-mantle boundary up to spherical harmonic degree 14 for imaging of the fluid flow below the core-mantle boundary. Here we present a method that combines helical flow and tangential geostrophy to obtain the fluid motion below the core-mantle boundary consistent with the secular variation. We compare results from different types of physical assumptions, such as tangential geostrophy, strong helicity, weak helicity and columnar flow.

Our solution method is novel in several respects. First, we formulate a general expression for the tangential divergence term that incorporates inertial effects such as tangential geostrophy with effects due to viscous and buoyancy forces that produce helical flow. Second, our method uses a grid-based finite difference representation, as opposed to the conventional spectral methods in which the flow potentials are represented in spherical harmonics.

* Corresponding author.
*E-mail address:* hagay@jhu.edu (H. Amit).

Non-uniqueness is a major problem in the inversion of fluid flow at the top of the core from geomagnetic secular variation data. Backus (1968) showed that, without specifying the tangential divergence, the flow is non-unique. Backus and LeMouël (1986) showed that the tangential geostrophy assumption reduces the non-uniqueness, but does not eliminate it. Our helical flow assumption removes this non-uniqueness.

The outline of the paper is as follows. In Section 2 we review the general theory and previous frozen flux inversions of geomagnetic secular variation. In Section 3 we describe the theoretical background for our method, including our physical assumptions. In Section 4 we describe our numerical technique and present results of a test case to verify its reliability. In Section 5 we present our results, including a sensitivity test, a resolution test and comparison between results from different physical assumptions. Our main findings are summarized in Section 6.

## 2. Frozen flux theory

### 2.1. The radial magnetic induction equation at the top of the core

Properties of the flow in the liquid outer core are inferred from geomagnetic secular variation, assuming the magnetic field acts like a tracer. The radial component of the magnetic induction equation is

$$\frac{\partial B_r}{\partial t} + \vec{u}_h \cdot \nabla B_r + B_r \nabla_h \cdot \vec{u}_h$$
$$= \lambda \left( \frac{1}{r^2} \frac{\partial^2}{\partial r^2} (r^2 B_r) + \nabla_h^2 B_r \right) \tag{1}$$

where $B_r$ is the radial component of the magnetic field, $t$ time, $\vec{u}_h$ the fluid velocity tangent to the core-mantle boundary, $\lambda$ the magnetic diffusivity and $\nabla_h^2 = \nabla^2 - 1/r^2 \, \partial/\partial r(r^2 \partial/\partial r)$. Throughout the paper, the subscript $h$ refers to tangential $(\theta, \phi)$ coordinates. To infer core flow using (1), the "tracer" $B_r$ and its time derivative $\partial B_r/\partial t$ are assumed known, and the fluid velocity $\vec{u}_h$ is unknown.

Previous studies generally assumed frozen flux, in which the diffusion of magnetic field is neglected in comparison with the advection of magnetic field by the flow. The frozen flux hypothesis is assumed valid

because the magnetic diffusion time scale, $\tau_\lambda = L^2/\lambda$, is much longer than the advection time, $\tau_v = L/U$, where $L$, $U$ and $\lambda$ are the typical length scale, velocity and magnetic diffusivity for the Earth's core. The ratio of these time scales in (1) yields

$$\frac{\tau_\lambda}{\tau_v} = \frac{|\vec{u}_h \cdot \nabla B_r|}{|\lambda \nabla_h^2 B_r|} \sim \frac{UL}{\lambda} = R_m \tag{2}$$

where $R_m$ is the magnetic Reynolds number. Using $L = 10^6$ m, $U = 5 \times 10^{-4}$ m/s and $\lambda = 1 \, \text{m}^2/\text{s}$ gives $\tau_\lambda \sim 30{,}000$ years and $\tau_v \sim 60$ years, i.e. $R_m \sim 500$, large enough so that the effects of magnetic diffusion can be neglected to a first approximation (e.g. Bloxham, 1989).

According to the Helmholtz representation, the tangential velocity can be written as the sum of a tangentially non-divergent toroidal velocity and a tangentially divergent poloidal velocity,

$$\vec{u}_h = \vec{u}_{\text{tor}} + \vec{u}_{\text{pol}} \tag{3}$$

In a spherical coordinate system $(r, \theta, \phi)$, the toroidal velocity can be expressed by a streamfunction $\Psi$ and the tangential poloidal velocity can be expressed by a scalar potential $\Phi$ in the following way:

$$\vec{u}_{\text{tor}} = \nabla \times \Psi \hat{r} \tag{4}$$

$$\vec{u}_{\text{pol}} = \nabla_h \Phi \tag{5}$$

where $\hat{r}$ is a unit radial vector. In terms of their components, the toroidal and poloidal tangential velocities are

$$(u_\theta, u_\phi)_{\text{tor}} = \left( \frac{1}{r \sin \theta} \frac{\partial \Psi}{\partial \phi}, -\frac{1}{r} \frac{\partial \Psi}{\partial \theta} \right) \tag{6}$$

$$(u_\theta, u_\phi)_{\text{pol}} = \left( \frac{1}{r} \frac{\partial \Phi}{\partial \theta}, \frac{1}{r \sin \theta} \frac{\partial \Phi}{\partial \phi} \right) \tag{7}$$

Using these expressions for the velocities, the radial vorticity in the fluid $\zeta$ is given in terms of the streamfunction $\Psi$ as

$$\zeta = \hat{r} \cdot \nabla \times \vec{u}_h = \nabla_h^2 \Psi \tag{8}$$

and the surface divergence of the fluid velocity $\nabla_h \cdot \vec{u}_h$ is given in terms of the scalar potential $\Phi$ as

$$\nabla_h \cdot \vec{u}_h = \nabla_h^2 \Phi \tag{9}$$

Substitution of (6), (7) and (9) into (1) and neglecting magnetic diffusion gives the radial component of the

frozen flux magnetic induction equation in terms of the two potentials $\Psi$ and $\Phi$. On the core-mantle boundary ($r = R$, the radius of the core), (1) becomes

$$\frac{\partial B_r}{\partial t} + \frac{1}{R^2 \sin \theta} \left( \frac{\partial \Psi}{\partial \phi} \frac{\partial B_r}{\partial \theta} - \frac{\partial \Psi}{\partial \theta} \frac{\partial B_r}{\partial \phi} \right)$$
$$+ \frac{1}{R^2} \left( \frac{\partial \Phi}{\partial \theta} \frac{\partial B_r}{\partial \theta} + \frac{1}{\sin^2 \theta} \frac{\partial \Phi}{\partial \phi} \frac{\partial B_r}{\partial \phi} \right) + B_r \nabla_h^2 \Phi = 0$$
(10)

The physical interpretation of the terms in (10) are as follows. The first term is the secular variation of the magnetic field. The second and third terms are advection of $B_r$ by toroidal and poloidal velocities, respectively. The fourth term represents the effect of upwelling motions from the interior of the outer core on $B_r$.

The core-mantle boundary is usually modeled a rigid impermeable boundary, in which case the velocity there is identically zero. However, since $B_r$ is continuous there, it is assumed that $B_r$ and $\partial B_r / \partial t$ vary little through the boundary layer, and (10) applies to the flow of the free stream at the top of the core just below the core-mantle boundary (Bloxham and Jackson, 1991).

## 2.2. Previous studies

Different core flows were obtained in the past due to different regularization methods, physical assumptions, and data (see Bloxham and Jackson, 1991 for a review of these). Previously-used spectral methods minimized simultaneously the data residual and a quadratic function of the parameter vector using a trade-off damping coefficient. Some previous studies have minimized the kinetic energy to regularize their solutions (Whaler, 1986; Gubbins, 1982). Others minimized the norm of the second derivatives of the flow (Bloxham, 1989), or the deviation from a decreasing velocity spectra (Gire and LeMouël, 1990). Pais and Hulot (2000) used a regularized method with one covariance matrix for the data uncertainty and another for the a-priori kinetic energy. They found a small range of damping coefficients which lead to a misfit in the data residual in agreement with the data uncertainty, and complies with the energetic requirement.

Previous authors truncated their flow solutions at some spherical harmonic degree. Gire et al. (1986)

derived a low spherical harmonic degree spectrum of motion. Whaler (1986) pointed out that the disadvantage of previous methods is strong dependency on the velocity truncation level. Rau et al. (2000) tested their inversion method with synthetic data from dynamo simulations. For their low-pass filter case, they resolved the flow up to spherical harmonic degree 5. They concluded that limited resolution due to crustal magnetization, uncertainties in the physical assumptions, and uncertainties in the methodical constraints lead to poorly constrained flows.

Different methods and physical assumptions have been used to reduce the non-uniqueness. Gubbins (1982) assumed a combination of steady flow without upwelling. He argued that the non-uniqueness is reduced if two separate inversions yield two sufficiently different directions of velocity. Voorhies (1986) used the steady flow assumption and pointed out that the non-uniqueness is reduced if $B_r$ at three different epochs is known. Rau et al. (2000) argued that the steady flow assumption yields poor fits even in decadal timescales. Another common way to reduce the non-uniqueness is by specifying the tangential divergence term in (1). The simplest upwelling assumption is, of course, pure toroidal flow: $\nabla_h \cdot \vec{u}_h = 0$. Without upwelling the non-unique flow component is along $B_r$-contours. Whaler (1980) interpreted relatively small secular variation values at local extrema of $B_r$ as statistical evidence for pure toroidal flow. Other authors have also concluded that the flow at the top of the core is purely toroidal. Gubbins (1982) interpreted the apparent upwellings in core flow models as data uncertainties, while Bloxham (1989) interpreted them as contamination by radial magnetic diffusion. LeMouël (1984) assumed tangential geostrophy from the balance between Coriolis and pressure gradient forces below the core-mantle boundary: $\nabla_h \cdot (\vec{u}_h \cos \theta) = 0$. For this assumption the non-unique flow component is along $B_r / \cos \theta$-contours that do not cross the equator. These ambiguous patches compose 40% of the core-mantle boundary at 1980 (Bloxham and Jackson, 1991; Chulliat and Hulot, 2000). Rau et al. (2000) concluded that the flow is mostly toroidal and geostrophic. Recent studies by Pais and Hulot (2000) and Hulot et al. (2002) preferred the tangential geostrophy assumption.

Some of the main inferences about core flow from previous studies are as follows. Voorhies (1986) found in pure toroidal flow solutions evidence for Taylor

columns in asymmetric vortices with respect to the equator. Some studies found that pure toroidal flows had better fits than geostrophic flows (Bloxham, 1989; Bloxham and Jackson, 1991). Bloxham (1989) observed persistent trans-equatorial flow below Indonesia, in contradiction to the geostrophic assumption. Whaler (1986) stated that any solution without upwelling yields a statistically inadequate fit. She remarked that upwelling indicates local convection strength. A poloidal–toroidal flow solution contains twice as many free parameters as a toroidal flow, and thus allows smaller data residuals. Authors that preferred poloidal–toroidal flow over pure toroidal flow argued that the first is less energetic (Gire et al., 1986), or its data residuals are significantly smaller (Voorhies, 1986). However, the poloidal flow component is less well determined (Whaler, 1986; Voorhies, 1986). Gire and LeMouël (1990) found an equatorially-aligned flow compatible with their geostrophic assumption. Rau et al. (2000) found both toroidal and geostrophic assumptions reasonable, with a preference for the latter. Gire and LeMouël (1990) concluded that the secular variation reflects the temporal behavior of the poloidal flow, and the toroidal flow is responsible for exchanging angular momentum between the core and the mantle. Jault et al. (1988) and Jackson et al. (1993) found good correlation between changes in the angular momentum of the core (inferred from core flow inversions) to those inferred from variations in the length of the day. Zatman and Bloxham (1997) interpreted time-dependent zonal flows as torsional oscillations. Rau et al. (2000) stressed that the limitation on the data resolution due to crustal magnetization might cause flow patterns with artifacts. They found that large scale zonal flow and mid-latitude gyres are the most reliable flow structures, and that they may represent an image of columnar convection outside the tangent cylinder, which is the imaginary cylinder parallel to the spin axis and circumscribing the equator of the inner core (Aurnou et al., 2003). Hulot et al. (2002) used the 2000 Oersted and 1980 Magsat satellite geomagnetic data sets and found higher velocities in the Atlantic hemisphere than in the Pacific one. They commented that the large secular variations at high latitudes (especially in the northern hemisphere) and below Africa could not be predicted before the Oersted data. Their non-axisymmetric flow displays vortices around the tangent cylinder.

Different authors' core flows contain different zonal flows. Gire et al. (1984) found that a 0.2°/year westward drift is the dominant flow motion. Bloxham (1989) found a westward drift less than 0.1°/year. The solution of Voorhies (1986) contains a bulk westward drift with superimposed jets and gyres. Pais and Hulot (2000) found large zonal angular velocities at high latitudes (though not reliable) and an equatorially-antisymmetric zonal flow outside the tangent cylinder. Hulot et al. (2002) found a westward equatorially-symmetric flow of ∼0.1°/year outside the tangent cylinder, and westward polar vortices of ∼0.9°/year. A similar polar vortex was found by Olson and Aurnou (1999).

## 3. Physical assumptions for coupling toroidal and poloidal motions

Eq. (10) contains two scalar variables, the potentials $\Psi$ and $\Phi$. In order to invert this equation for the tangential velocity at the top of the free stream below the core-mantle boundary given $B_r$ and $\partial B_r / \partial t$, we make one additional assumption to relate the two potentials. We will show that this assumption removes the non-uniqueness from the inversion problem.

### 3.1. Pure toroidal flow

A trivial way to couple toroidal and poloidal flows is to assume that the flow is purely toroidal, so that

$$\nabla_h \cdot \vec{u}_h = 0 \qquad (11)$$

According to this assumption, the surface flow is non-divergent and can be expressed in terms of the streamfunction only, i.e. all terms with $\Phi$ in (10) vanish.

### 3.2. Tangential geostrophy

Another standard way to couple toroidal and poloidal flows is to assume a geostrophic balance for the tangential components of the fluid momentum below the core-mantle boundary, i.e. Coriolis and pressure gradient forces dominate the flow (LeMouël, 1984). This is the tangential geostrophy assumption, and leads to the following constraint:

$$\nabla_h \cdot (\vec{u}_h \cos \theta) = 0 \qquad (12)$$

which can be rewritten as

$$\cos\theta\,\nabla_h\cdot\vec{u}_h + \vec{u}_h\cdot\nabla\cos\theta = 0 \qquad (13)$$

The expression for the radial upwelling becomes, according to the tangential geostrophy assumption

$$\nabla_h\cdot\vec{u}_h = \frac{\tan\theta}{R}u_\theta \qquad (14)$$

which can be expressed in terms of the two potentials $\Psi$ and $\Phi$ using (6), (7) and (9) as

$$\nabla_h^2\Phi = \frac{\tan\theta}{R^2}\left(\frac{1}{\sin\theta}\frac{\partial\Psi}{\partial\phi} + \frac{\partial\Phi}{\partial\theta}\right) \qquad (15)$$

### 3.3. Helical flow

Here we introduce a third way to couple toroidal and poloidal motions, by assuming a correlation between tangential divergence and radial vorticity at the top of the free stream below the core-mantle boundary. We assume

$$\nabla_h\cdot\vec{u}_h = \mp k_0\zeta \qquad (16)$$

where $\zeta$ is the radial vorticity and $k_0$ is a positive constant. Eq. (16) can be rewritten in terms of the potentials $\Psi$ and $\Phi$ using (8) and (9) as

$$\nabla_h^2\Phi = \mp k_0\nabla_h^2\Psi \qquad (17)$$

The negative signs in (16) and (17) apply to the northern hemisphere, and the positive signs apply to the southern hemisphere. The sign difference in those two expressions is attributed to the Coriolis force which deflects motions to the right in the northern hemisphere and to the left in the southern hemisphere. Therefore, upwelling is associated with clockwise motion (negative vorticity) in the northern hemisphere and with anticlockwise motion (positive vorticity) in the southern hemisphere.

The type of correlation in (16) and (17) can be viewed as the surface expression of a three-dimensional flow which has the kinematic property of helicity, defined as

$$H = \vec{\zeta}\cdot\vec{u} \qquad (18)$$

where $H$ is the helicity, $\vec{\zeta}$ the vorticity vector and $\vec{u}$ is the three-dimensional velocity. According to (18), helicity appears in flows where there is a correlation between vorticity and velocity vectors. Often (but not always) the toroidal (or rotational) component of the motion is responsible for the radial vorticity and the poloidal (or convective) component of the motion is responsible for the radial velocity. We call this type of motion the *helical flow assumption* (16). We note that although the helicity vanishes on approach to the core-mantle boundary, the existence of upwelling motion correlated with vorticity implies non-zero helicity at greater depths.

### 3.4. Columnar flow

A fourth way to couple toroidal and poloidal motions is to assume a columnar-type flow. According to the Taylor–Proudman theorem, in a purely columnar flow the velocity does not vary in the direction parallel to the rotation, i.e.

$$(\vec{\Omega}\cdot\nabla)\vec{u} = 0 \qquad (19)$$

where $\vec{u}$ is again the full velocity vector and $\vec{\Omega}$ is the rotation vector. In a sphere, the curved boundaries do not allow the flow to be entirely independent of the $\vec{\Omega}$-direction. Still, the columnar nature of motions remains a characteristic feature in convection in rapidly rotating fluid spheres (Busse, 1975), where these types of flow structures are known as "Busse columns". Linear adjustment of columnar flow to spherical boundaries yields the following upwelling term:

$$\nabla_h\cdot\vec{u}_h = \frac{2\tan\theta}{R}u_\theta \qquad (20)$$

A full development of (20) is given in Appendix A. Note that this expression differs from the tangential geostrophy upwelling expression (14) only by the factor 2. Eq. (20) can be rewritten in terms of the two potentials $\Psi$ and $\Phi$ using (6), (7) and (9) as

$$\nabla_h^2\Phi = \frac{2\tan\theta}{R^2}\left(\frac{1}{\sin\theta}\frac{\partial\Psi}{\partial\phi} + \frac{\partial\Phi}{\partial\theta}\right) \qquad (21)$$

### 3.5. Upwelling relationships in geophysical fluids

Because there is no way to directly determine the relationship between $\Psi$ and $\Phi$ at the top of the Earth's core, we look to other geophysical fluid systems for insight. Here we discuss several examples of upwelling flows commonly found in rotating fluids.

### 3.5.1. Examples of tangential geostrophy

Examples of tangential geostrophy are found in both the ocean and the atmosphere. In the subtropical ocean, the interior flow is governed by the Sverdrup relation (Sverdrup, 1947; Salmon, 1998)

$$\nabla_h \cdot \vec{u}_h = -\frac{\beta}{f} u_\theta \tag{22}$$

where $\theta$ is co-latitude. The Coriolis parameter $f$ and its rate of change with co-latitude $\beta$ are defined as

$$f = 2\Omega \cos \theta \tag{23}$$

$$\beta = \frac{\partial f}{\partial y} = \frac{\partial f}{\partial \theta} \frac{\partial \theta}{\partial y} = -\frac{2\Omega \sin \theta}{R} \tag{24}$$

where $y$ is the local Cartesian northward coordinate, $\Omega$ the Earth's rotation rate and $R$ is the radius. Substitution of (23) and (24) into (22) yields

$$\nabla_h \cdot \vec{u}_h = \frac{2\Omega \sin \theta}{2R\Omega \cos \theta} u_\theta = \frac{\tan \theta}{R} u_\theta \tag{25}$$

Eq. (25) is identical to (14), i.e. the Sverdrup relation is equivalent to the tangential geostrophy assumption. Similar correlation between tangential divergence and meridional velocity was also reported by Sardeshmukh and Hoskins (1987, 1988) for solutions to the vorticity equation in the tropical atmosphere.

### 3.5.2. Examples of helical flow

There are numerous examples of helical flow in rotating fluids. In the atmosphere for example, a high/low pressure (in the northern hemisphere) is associated with a clockwise/anticlockwise circulation, according to the geostrophic balance. Deviation from this balance due to friction at the ground yields downwelling/upwelling. Therefore, the divergence of the tangential motion is correlated with the vorticity in the vertical direction. Velocity/vorticity correlation appears in observations and in numerical simulations of atmospheric tropical cyclones. Lilly (1986) found that long-lived stable rotating storms in the atmosphere are characterized by large values of helicity in both the storms and their surrounding environment.

Helicity and the type of correlation in (16) are also found in rotating convection. For example, at the onset of thermal convection in a plane layer of high Prandtl number fluid heated from below with rotation in the presence of a uniform vertical magnetic field, the instability sets in as stationary convection. For the case of convection between two free horizontal boundaries, the depth-dependent vertical velocity, tangential divergence and vertical vorticity are given by (Chandrasekhar, 1961)

$$w = \pm w_0 \sin\left(\frac{\pi z}{d}\right) \tag{26}$$

$$\nabla_h \cdot \vec{u}_h = \mp w_0 \frac{\pi}{d} \cos\left(\frac{\pi z}{d}\right) \tag{27}$$

$$\zeta = \left(\frac{1}{dE}\right) \frac{\pi(\pi^2 + a^2)}{(\pi^2 + a^2)^2 + Q\pi^2} w_0 \cos\left(\frac{\pi z}{d}\right) \tag{28}$$

where $z$ is the vertical Cartesian coordinate (antiparallel to gravity), $d$ the depth of the fluid layer, $w_0$ the vertical velocity at $z = d/2$, $a$ the non-dimensional convection cell width ($a = kd$ where $k$ is the wave number), $E$ the Ekman number (the ratio between viscous to rotation forces) and $Q$ is the Chandrasekhar number (the ratio between magnetic to viscous forces). The upper sign in (26) and (27) applies to a northern hemisphere geometry (anticlockwise rotation of the fluid layer) and the lower sign applies to a southern hemisphere geometry (clockwise rotation of the fluid layer). The helicity for this flow is found by substituting (26) and (28) into (18),

$$H = \pm \left(\frac{1}{dE}\right) \frac{\pi(\pi^2 + a^2)}{(\pi^2 + a^2)^2 + Q\pi^2} w_0^2$$
$$\times \cos\left(\frac{\pi z}{d}\right) \sin\left(\frac{\pi z}{d}\right) \tag{29}$$

In this example the helicity depends on depth. At the boundaries ($z = 0, d$) and at midway ($z = d/2$) the helicity vanishes. In the northern hemisphere the helicity is negative/positive in the upper/lower half of the fluid layer, respectively. The ratio of the tangential divergence to the vertical vorticity is, from (27) and (28),

$$\frac{\nabla_h \cdot \vec{u}_h}{\zeta} = \mp k_0 = \mp E \left[\frac{(\pi^2 + a^2)^2 + Q\pi^2}{(\pi^2 + a^2)}\right] \tag{30}$$

Note that the divergence/vorticity ratio in (30) is independent of depth. In the northern hemisphere, at the lower/upper half of the fluid layer, convergence/divergence are associated with positive/negative vorticity, respectively.

Two special cases of (30) deserve special note in this context. First, in the case of no magnetic field ($Q = 0$,

i.e. purely rotating convection), $a \to (1/2\pi^2)^{1/6} E^{-1/3}$ in the limit of small Ekman number (Chandrasekhar, 1961). According to the Prandtl turbulence hypothesis all the effective diffusivities are equal, i.e., $\nu = \lambda = 1\,\text{m}^2/\text{s}$, therefore $E \simeq 10^{-9}$, and (30) gives $k_0 \simeq 10^{-3}$. Second, in the more general case where both rotation and magnetic field are present, $k_0$ is larger. For typical core values of $E \simeq 10^{-9}$ and $Q \simeq 10^9$, Chandrasekhar (1961) shows that $a \simeq \sqrt{1.5\pi}$ at the onset of convection. Substituting these values into (30) gives $k_0 \simeq 0.4$, within the range of values that we use in this paper.

Based on results from numerical dynamos, it has been proposed that helicity is present in convection in the outer core. Olson et al. (1999) found in dynamo simulations columnar convection with large amounts of helicity with opposite signs in the two hemispheres. Results of convective dynamo simulations display a constant of proportionality ($\sim$0.07) between the tangential divergence and the vertical vorticity of the fluid flow at the outer core just below the core-mantle boundary (Olson et al., 2002).

Another example of helical flow in rotating fluids is an Ekman boundary layer. The horizontal velocity components in a laminar Ekman layer with a top rigid boundary are, in a local Cartesian coordinate system (e.g. Kundu, 1990; Cushman-Roisin, 1994; Andrews, 2000)

$$u = U \left[ 1 - \text{e}^{z/\delta} \cos\left(\frac{z}{\delta}\right) \right] \tag{31}$$

$$v = \mp U \text{e}^{z/\delta} \sin\left(\frac{z}{\delta}\right) \tag{32}$$

where $u$ and $v$ are the $x$ (eastward) and $y$ (northward) velocity components respectively, $U$ is the $y$-dependent zonal velocity far from the boundary layer, and $z$ is the vertical coordinate directed out of the boundary, so that $z = 0$ at the boundary and $z < 0$ at the interior in (31) and (32). The negative sign in (32) applies in the northern hemisphere and the positive sign applies in the southern hemisphere. The thickness $\delta$ of the Ekman boundary layer is given by

$$\delta = \sqrt{\frac{2\nu}{|f_0|}} \tag{33}$$

where $\nu$ is the kinematic viscosity and $f_0 = 2\Omega \cos \theta_0$ the $f$-plane approximation to the Coriolis parameter, where $\Omega$ is the Earth's rotation rate and $\theta_0$ is the lo-

cal co-latitude. The depth-dependent horizontal divergence and vertical vorticity derived from (31) and (32) are

$$\nabla_h \cdot \vec{u}_h = \frac{\partial u}{\partial x} + \frac{\partial v}{\partial y} = \mp \frac{\partial U}{\partial y} \text{e}^{z/\delta} \sin\left(\frac{z}{\delta}\right) \tag{34}$$

$$\zeta = \frac{\partial u}{\partial y} - \frac{\partial v}{\partial x} = \frac{\partial U}{\partial y} \left[ 1 - \text{e}^{z/\delta} \cos\left(\frac{z}{\delta}\right) \right] \tag{35}$$

The depth-dependent vertical velocity associated with (34) is

$$w = -\int_z^0 \nabla_h \cdot \vec{u}_h(z')\,\text{d}z'$$
$$= \mp \frac{\delta}{2} \frac{\partial U}{\partial y} \left[ \text{e}^{z/\delta} \left( \sin\left(\frac{z}{\delta}\right) - \cos\left(\frac{z}{\delta}\right) \right) + 1 \right] \tag{36}$$

Substituting (35) and (36) into (18) gives the depth-dependent helicity of the flow through an Ekman boundary layer,

$$H = \zeta w = \mp \frac{\delta}{2} \left( \frac{\partial U}{\partial y} \right)^2 \left[ 1 - \text{e}^{z/\delta} \cos\left(\frac{z}{\delta}\right) \right]$$
$$\times \left[ \text{e}^{z/\delta} \left( \sin\left(\frac{z}{\delta}\right) - \cos\left(\frac{z}{\delta}\right) \right) + 1 \right] \tag{37}$$

From (34) and (35), the ratio between horizontal divergence and vertical vorticity in this case is

$$\frac{\nabla_h \cdot \vec{u}_h}{\zeta} = \mp k_0 = \mp \frac{\text{e}^{z/\delta} \sin(z/\delta)}{1 - \text{e}^{z/\delta} \cos(z/\delta)} \tag{38}$$

As in the previous example of rotating convection, the ratio between horizontal divergence and vertical vorticity (38) is independent of the tangential coordinates. In a rotating, convecting layer this ratio was also independent of depth, whereas in an Ekman boundary layer this ratio varies with depth. Fig. 1 shows the normalized helicity and the depth-dependent divergence/vorticity ratio for an Ekman boundary layer in the northern hemisphere geometry, according to (37) and (38). $H$ in (37) is negative/positive and the ratio in (38) is positive/negative throughout the northern/southern hemisphere, respectively. $k_0$ goes asymptotically to zero far from the boundary layer (practically vanishes at $z \simeq 3\delta$), and $k_0(z = \delta) = 0.39$. From Fig. 1 it is evident that $H$ and $k_0$ are anti-correlated. The helicity is large far from the boundary layer where velocity and vorticity correlate, and $k_0$ vanishes far from the boundary layer due to the lack of horizontal divergence there.
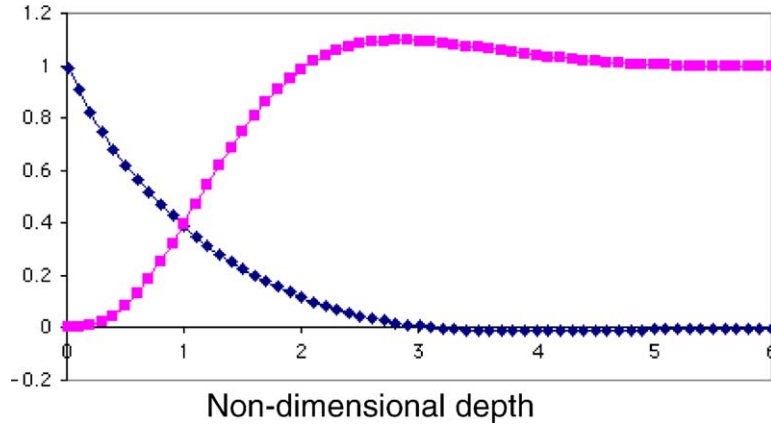
Fig. 1. Divergence/vorticity ratio and normalized helicity as a function of depth in an Ekman boundary layer in the southern hemisphere. Squares denote the ratio between tangential divergence to radial vorticity $k_0$ in (38), and diamonds denote the normalized helicity $-H/[(\delta/2)(\partial U/\partial y)^2]$ in (37).

The surface expression of such flow is large $k_0$ values due to the divergence/vorticity correlation, and the helicity vanishes at the surface where the flow becomes two dimensional. Thus, we use the term "helical" to describe a flow which has large helicity in the interior, and its surface expression is the correlation between tangential divergence and radial vorticity.

To summarize, the ratio between tangential divergence and radial vorticity in helical flow changes sign across the equator and is independent of the tangential coordinates in both an Ekman boundary layer and rotating, convecting layer. However, the depth dependence is different in the two situations. From these results, we infer that the parameter $k_0$ may be tangentially uniform in the core, but its depth-variation in the outer core is uncertain. Therefore we test different values of $k_0$. For upwelling models such as strong helicity, tangential geostrophy, and columnar flow, we use a small value of $k_0 = 0.1$. In our test case, this value yields an advective limit solution. We use $k_0 = 0.5$ for the weak helicity case to examine the effect of different $k_0$ values on our solution.

### 3.6. General upwelling relationship

The helical flow and tangential geostrophy upwelling terms can be superimposed, due to the linear relationship between geostrophic and boundary layer effects, similar to the superposition of pressure-driven and stress-driven horizontal velocities in an Ekman boundary layer. A general expression for the tangential divergence that incorporates the helical flow (17), tangential geostrophy (15), columnar flow (21) and pure toroidal flow (11) assumptions is

$$\nabla \cdot \vec{u}_h = \nabla_h^2 \Phi = \mp k_0 \nabla_h^2 \Psi$$
$$+ c \frac{\tan \theta}{R^2} \left( \frac{1}{\sin \theta} \frac{\partial \Psi}{\partial \phi} + \frac{\partial \Phi}{\partial \theta} \right) \qquad (39)$$

where the negative sign in the first term on the right hand side applies in the northern hemisphere and the positive sign in the same term applies in the southern hemisphere. Different values of $k_0$ and $c$ in (39) define all the physical assumptions discussed above: $k_0 = c = 0$ for pure toroidal flow, $k_0 = 0$ and $c = 1$ for tangential geostrophy, $k_0 \neq 0$ and $c = 0$ for helical flow, $k_0 = 0$ and $c = 2$ for columnar flow. Together, (39) and (10) constitute a set of two equations for the two unknowns, the potentials $\Psi$ and $\Phi$.

Two limits of (39) are worth noting. For large values of $k_0$ (and away from the equator), the first term on the right hand side in (39) is dominant, yielding a proportionality between surface divergence and radial vorticity. In this limit, poloidal velocity sources coincide with toroidal vortex centers. The other limit is for small values of $k_0$ (and at low latitudes). In this limit, the second term on the right hand side in (39), is dominant. This correlation produces centers of divergence where the meridional velocity is large.

### 3.7. Non-uniqueness and "invisible" flow

Non-uniqueness in the inversion of the magnetic induction equation occurs in situations where some component of the flow is "invisible", i.e. does not generate secular variation of its own (Backus and LeMouël, 1986). For pure toroidal flow, motions parallel to contours of $B_r$ are "invisible". For tangential geostrophy, the flow is "invisible" along contours of $B_r / \cos \theta$ which do not cross the equator (Chulliat and Hulot, 2000). Therefore, both assumptions have "invisible" flows, but the non-uniqueness in tangential geostrophy is confined to ambiguous patches and is more restricted than in pure toroidal flow.

Here we derive an equation governing the "invisible" motion with the helical flow assumption included. According to (1), the "invisible" flow consistent with the frozen flux magnetic induction equation obeys

$$\nabla_h \cdot (B_r \vec{u}_h^{\mathrm{i}}) = 0 \tag{40}$$

where $\vec{u}_h^{\mathrm{i}}$ denotes the "invisible" flow. The tangentially non-divergent vector $B_r \vec{u}_h^{\mathrm{i}}$ can be expressed in terms of a scalar potential $\Gamma$ as follows (Backus, 1968; Backus and LeMouël, 1986):

$$B_r \vec{u}_h^{\mathrm{i}} = \nabla \times \Gamma \hat{r} \tag{41}$$

According to (41), the tangential divergence of the "invisible" flow is given by

$$\nabla_h \cdot \vec{u}_h^{\mathrm{i}} = \frac{1}{B_r^2 R^2 \sin \theta} \left( \frac{\partial B_r}{\partial \phi} \frac{\partial \Gamma}{\partial \theta} - \frac{\partial B_r}{\partial \theta} \frac{\partial \Gamma}{\partial \phi} \right) \tag{42}$$

Eq. (39) can be written using the "invisible" flow components:

$$\nabla_h \cdot \vec{u}_h^{\mathrm{i}} = \mp k_0 \hat{r} \cdot \nabla \times \vec{u}^{\mathrm{i}} + c \frac{\tan \theta}{R} u_\theta^{\mathrm{i}} \tag{43}$$

Substitution of the "invisible" velocity components defined in (41) into the right hand side of (43), equating with the right hand side of (42), and rearranging, yields

$$\left( \frac{\partial B_r}{\partial \phi} \pm k_0 \sin \theta \frac{\partial B_r}{\partial \theta} \right) \frac{\partial \Gamma}{\partial \theta}$$
$$- \left( \frac{\partial B_r}{\partial \theta} + c B_r \tan \theta \mp k_0 \frac{1}{\sin \theta} \frac{\partial B_r}{\partial \phi} \right) \frac{\partial \Gamma}{\partial \phi}$$
$$= \pm k_0 B_r R^2 \sin \theta \nabla_h^2 \Gamma \tag{44}$$

an equation for the scalar $\Gamma$ with spatially-variable coefficients. For pure toroidal flow (i.e. $k_0 = c = 0$), the solution to (44) is $\Gamma = B_r$, and for tangential geostrophy (i.e. $k_0 = 0$, $c = 1$), the solution is $\Gamma = B_r / \cos \theta$, as expected. For combined helical flow and tangential geostrophy (i.e. $k_0 \neq 0$, $c = 1$), (44) is an elliptic partial differential equation. According to the maximum principle of E. Hopf, a non-constant solution of equations of this type can attain neither a maximum nor a minimum at an interior point (Protter and Weinberger, 1967). All points are interior on a surface of a sphere, so that only the trivial solution, $\Gamma = constant$, exists. Therefore, the "invisible" flow defined by (41) is identically zero, i.e. the non-uniqueness associated with "invisible" flow is removed when helical flow is included. This is a reason why solutions with the helical flow assumption may contain more flow along $B_r$-contours than do previous solutions.

## 4. Numerical method

For numerical solution, we rewrite (10) and (39) as advection-diffusion equations for $\Psi$ and $\Phi$ of the form

$$\frac{\partial \Psi}{\partial \tau} = \frac{\partial B_r}{\partial t} + \frac{1}{R^2 \sin \theta} \left( \frac{\partial \Psi}{\partial \phi} \frac{\partial B_r}{\partial \theta} - \frac{\partial \Psi}{\partial \theta} \frac{\partial B_r}{\partial \phi} \right)$$
$$+ \frac{1}{R^2} \left( \frac{\partial \Phi}{\partial \theta} \frac{\partial B_r}{\partial \theta} + \frac{1}{\sin^2 \theta} \frac{\partial \Phi}{\partial \phi} \frac{\partial B_r}{\partial \phi} \right) + B_r \nabla_h^2 \Phi$$
$$\tag{45}$$

$$\frac{\partial \Phi}{\partial \tau} = \nabla_h^2 \Phi - \left( \mp k_0 \nabla_h^2 \Psi + c \frac{\tan \theta}{R^2} \right.$$
$$\left. \times \left( \frac{1}{\sin \theta} \frac{\partial \Psi}{\partial \phi} + \frac{\partial \Phi}{\partial \theta} \right) \right) \tag{46}$$

where $\tau$ is a relaxation variable and $\partial B_r / \partial t$ is the source term. In (46), the coefficient $-k_0$ applies in the northern hemisphere, and $+k_0$ applies in the southern hemisphere. We use $B_r$ and $\partial B_r / \partial t$ on the core-mantle boundary in (45) and (46), but like previous authors, we interpret $\Psi$ and $\Phi$ at the top of the free stream below the core-mantle boundary. We solve (45) and (46) simultaneously for the two potentials $\Psi$ and $\Phi$ using an iterative technique, starting from initial conditions $\Psi = \Phi = 0$. The Laplacian operators act to diffuse the residuals in (45) and (46) and allow the spatial variations

of the time-like derivatives $\partial\Psi/\partial\tau$ and $\partial\Phi/\partial\tau$ to converge after a certain number of iterations. We use a second order, central finite difference method on regular $5° \times 5°$ and in one case $2.5° \times 2.5°$ grids that avoid the two poles and the equator. To verify that non-uniqueness is practically removed, we solved (45) and (46) using different initial conditions and obtained the same final solutions.

It is well known that finite difference methods in spherical coordinates often have problems at the poles. We treat the polar points as follows. We calculate the derivatives of the potentials $\Psi$ and $\Phi$ at the latitude points closest to the poles, using the value of $\Psi$ and $\Phi$ at the polar point itself in the finite difference formulas. The values at the poles are then re-calculated as the average of the values of the potentials over the closest latitude grid line. With this method, streamlines are free to cross (or not to cross) the poles.

The equator requires special treatment for the last term in (46), which is singular there. For $c \neq 0$, (10)

and (39) at the equator reduce to

$$\left.\frac{\partial\Psi}{\partial\phi}\right|_{eq} = -\left.\frac{\partial\Phi}{\partial\theta}\right|_{eq} \tag{47}$$

We add an hypothetical equatorial grid line to enforce (47). Cross-equator values are used to calculate $\partial\Phi/\partial\theta$, and then (47) is integrated to obtain $\Psi$ on the equator. The equatorial $\Psi$-values found this way are then used to calculate $\partial\Psi/\partial\theta$ and $\partial^2\Psi/\partial\theta^2$ at latitudes nearest to the equator. We further approximate the last term in (46) on the nearest latitudes to the equator using (47), which becomes

$$\left.\frac{\partial\Phi}{\partial\tau}\right|_{eq} = \nabla_h^2 \Phi|_{eq}$$

$$- \left.\left(\mp k_0 \nabla_h^2 \Psi + c\frac{\tan\theta}{R^2}\left(\frac{1}{\sin\theta}-1\right)\frac{\partial\Psi}{\partial\phi}\right)\right|_{eq} \tag{48}$$



Fig. 2. Streamfunction for the test case of a dipole magnetic field with instantaneous pole at $[\phi_0, \theta_0] = [0, 45\,\text{N}]$ and rotating perpendicular to the equatorial plane and parallel to the $\phi_0 = 0$ longitude line at a constant angular velocity $\omega = 1°/\text{year}$, with $k_0 = 0.1$.

Our finite difference relaxation solution method has some limitations. The coefficient $\mp k_0 B_r$, which acts like a spatially-variable streamfunction diffusivity, has to exceed some minimum value that depends on the grid size in order to reach numerical convergence. Furthermore, $\mp k_0 B_r$ must maintain the same sign over the entire grid, otherwise locally negative diffusivity will produce numerical instability in those regions. To overcome these limitations, we use a smoothed version for $B_r$ only for the last term on the right hand side of (45), to guarantee numerical stability in the vicinity of null flux areas where $B_r = 0$ and inside reversed flux patches where $B_r$ changes sign.

### 4.1. Test case

In order to verify the reliability of our method, we examine solutions of a synthetic test case. We choose the simple case of a dipole magnetic field with its pole located at latitude $\theta_0$ and longitude $\phi_0 = 0$, rotating along the longitude $\phi_0 = 0$ at constant angular velocity $\omega$. The instantaneous radial magnetic field for this case is given by

$$B_r = \cos(\theta_0 + \omega t) \cos \theta$$
$$+ \sin(\theta_0 + \omega t) \sin \theta \cos \phi \quad (49)$$

and the secular variation induced by the rotation is

$$\frac{\partial B_r}{\partial t} = -\omega \sin(\theta_0 + \omega t) \cos \theta$$
$$+ \omega \cos(\theta_0 + \omega t) \sin \theta \cos \phi \quad (50)$$

The streamfunction found by substituting (49) and (50) into (45) and (46) using $k_0 = 0.1$, $c = 0$, $\omega = 1°$/year and $\theta_0 = 45$ N is shown in Fig. 2. This map conforms to the expected pattern of uniform rotation perpendicular to the equatorial plane and parallel to the $\phi_0 = 0$ longitude. The magnitude of the flow is also nearly correct; the average angular velocity has an error of 3.2%, compatible to the discretization error on the $5° \times 5°$ grid.
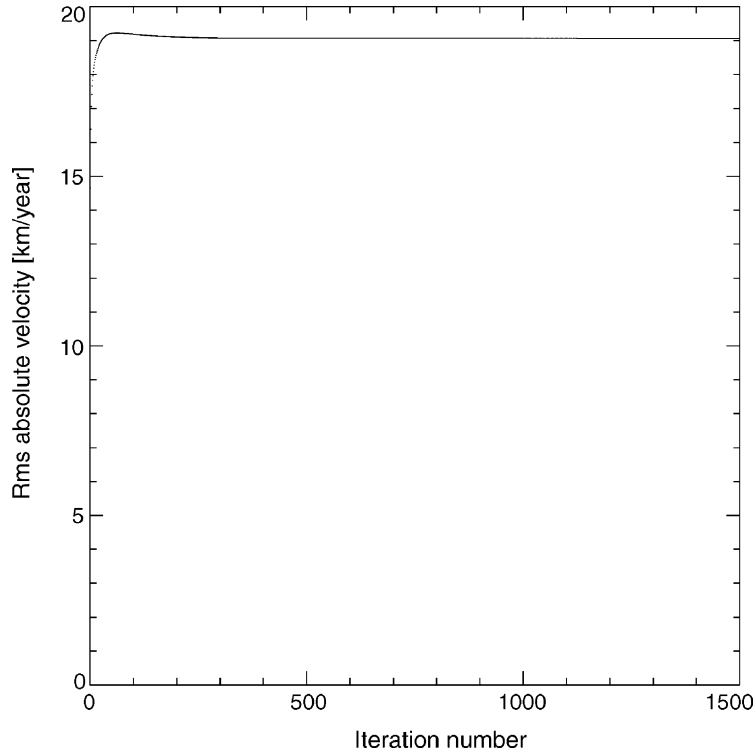


Fig. 3. rms absolute velocity as a function of iteration number for the tangential geostrophy case 1. The asymptotic curve verifies numerical convergence.

Various values of $\omega$ and $\theta_0$ were tested and produced similar results to those shown in Fig. 2 in terms of accuracy of pattern and magnitude. This test case verifies the convergence of (45) for $\Psi$ in its advective limit, i.e., small amounts of streamfunction diffusion ($k_0 = 0.1$) stabilize the solution and only slightly modify the pure toroidal character of the flow. To verify the convergence of (46), we check that $\Psi$ satisfies the tangential divergence expression (39). We have also verified this convergence in each of our real data cases.

Fig. 3 demonstrates the convergence of the solution for our main flow case (which will be defined and discussed below). We plot the rms absolute velocity over the entire grid as a function of iteration number, which shows the convergence to an asymptotic value.

## 5. Core flow cases

Fig. 4 shows the radial geomagnetic field and secular variation models on the core-mantle boundary from the 2000 Oersted and 1980 Magsat satellites, truncated at spherical harmonic degree 14. The magnetic field model for 1990 in Fig. 4 is the average of the Oersted and the Magsat field models, and the secular variation at 1990 is their difference divided by 20 years. These field
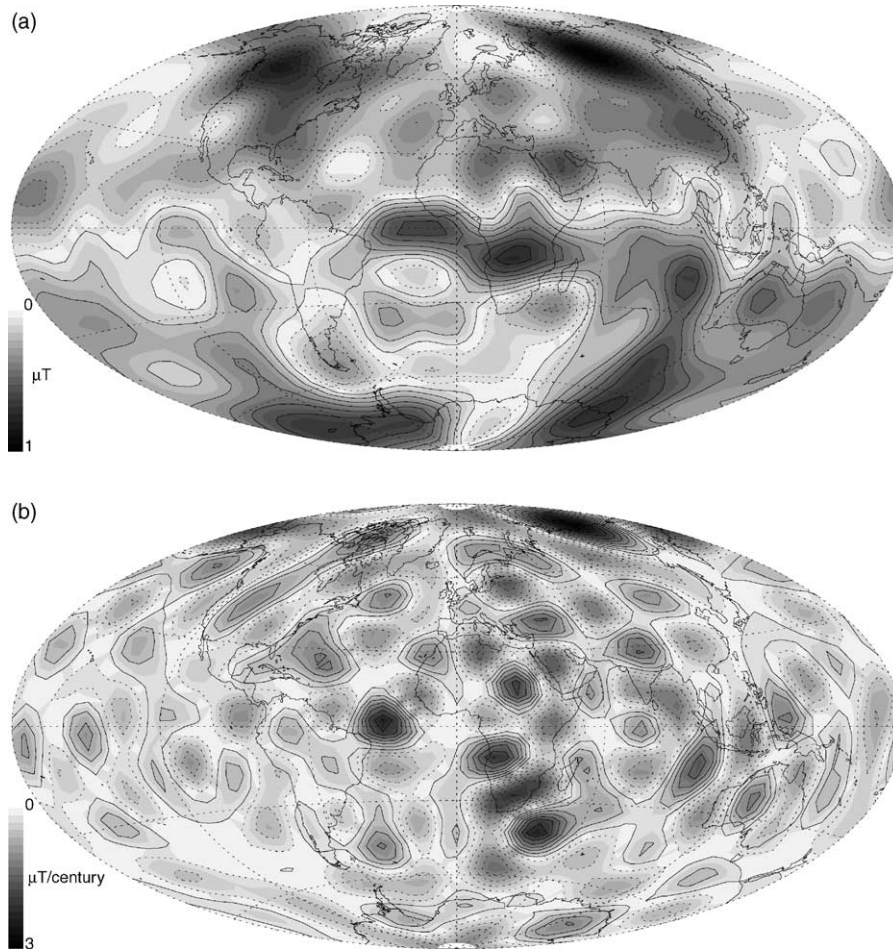


Fig. 4. Radial magnetic field (a) and secular variation (b) in 1990 on the core-mantle boundary. Grey scale represents absolute values, solid lines are positive, dotted lines are negative. The 1990 magnetic field is the average of the 2000 Oersted and 1980 Magsat field models, and the secular variation is their difference divided by 20 years.

Table 1
Maximum and mean velocities for different cases

| Case | Characterization | $k_0$ | $c$ | $\Delta$ | Maximum values (km/year) | | | rms values (km/year) | | |
|---|---|---|---|---|---|---|---|---|---|---|
| | | | | | $u_{tor}$ | $u_{pol}$ | $u_{abs}$ | $u_{tor}$ | $u_{pol}$ | $u_{abs}$ |
| 1 | Tangential geostrophy | 0.1 | 1 | 5 | 84.6 | 33.5 | 79.9 | 19.0 | 3.9 | 19.4 |
| 2 | Sensitivity test | 0.1 | 1 | 5 | 41.5 | 10.2 | 49.6 | 11.8 | 2.9 | 12.1 |
| 3 | Resolution test | 0.1 | 1 | 2.5 | 134.0 | 33.9 | 141.4 | 26.3 | 6.0 | 26.9 |
| 4 | Strong helicity | 0.1 | 0 | 5 | 83.0 | 36.3 | 84.2 | 21.0 | 2.2 | 21.1 |
| 5 | Weak helicity | 0.5 | 0 | 5 | 22.8 | 11.7 | 25.6 | 6.2 | 3.1 | 6.9 |
| 6 | Columnar flow | 0.1 | 2 | 5 | 130.3 | 46.8 | 173.4 | 21.7 | 8.5 | 22.2 |

$k_0$ and $c$ values refer to Eq. (39), $\Delta$ is grid size in degrees.

models were used in (45) and (46) to obtain flow maps that correspond to the cases described above: tangential geostrophy, strong and weak helicity, and columnar flow.

Table 1 defines the different flow cases and summarizes the core-mantle boundary surface rms and maximum values for the various solutions. The values of $k_0$ and $c$ define the various upwelling models used in each case, according to (39). The characterization in Table 1 identifies the most important among the different terms in the upwelling expression for each case. In case 1, a small value of $k_0$ and $c = 1$ indicates that tangential geostrophy is dominant. In case 2, the sensitivity of the method is investigated by using a filtered model for the secular variation with the same upwelling model as in case 1. In case 3, we examine the effects of grid resolution using the same upwelling model as in case 1 but on a finer grid. In case 4, a small value of $k_0$ and $c = 0$ simulates flow with strong helicity. In case 5, a relatively large $k_0$ value is used in order to provide the effect of weak helicity. In case 6, a small value of $k_0$ and $c = 2$ means that columnar flow is the dominant source of upwelling. Surface rms values are the surface average of the absolute pointwise values, and maximum values are the maximum absolute values. The quantities $u_{tor}$, $u_{pol}$ and $u_{abs}$ denote the toroidal, poloidal and absolute velocities, respectively.

The quality of convergence is defined by two misfits. The first is the data misfit, defined as the ratio of the rms data residual $\langle \partial \Psi / \partial \tau \rangle$ to the rms secular variation $\langle \partial B_r / \partial t \rangle$ over the entire grid. The second is the divergence misfit, the ratio of the rms tangential divergence residual $\langle \partial \Phi / \partial \tau \rangle$ to the rms tangential divergence $\langle \nabla_h^2 \Phi \rangle$ over the entire grid. Table 2 summarizes the quality of the different solutions in terms of their misfits.

We begin by describing our tangential geostrophy solution (case 1) and we compare it to tangential geostrophy solutions previously obtained by others. We then use a sensitivity test to demonstrate the robustness of our solution method with respect to small-scale variations in the data (case 2). We then show a resolution test in which we re-solve case 1 on a finer grid. We compare the flows from cases 1, 4–6 to investigate the effect of different upwelling models. Finally, we focus on some areas in case 1 that illustrate different kinematic scenarios which lead to the observed secular variation at the core-mantle boundary.

## 5.1. Tangential geostrophy case

Fig. 5a shows the flow map for the tangential geostrophy case. We name this case "tangential geostrophy" due to the dominance of the tangential geostrophy assumption in (16), even though the upwelling model in this case also includes the helical flow term. The dominant features in the solution are a large anticlockwise circulation in the southern hemisphere centered beneath southern Africa and Antarctica, a strong clockwise vortex centered below Bermuda, and a westward drift sweeping most of the Atlantic southern

Table 2
Misfit values for different cases

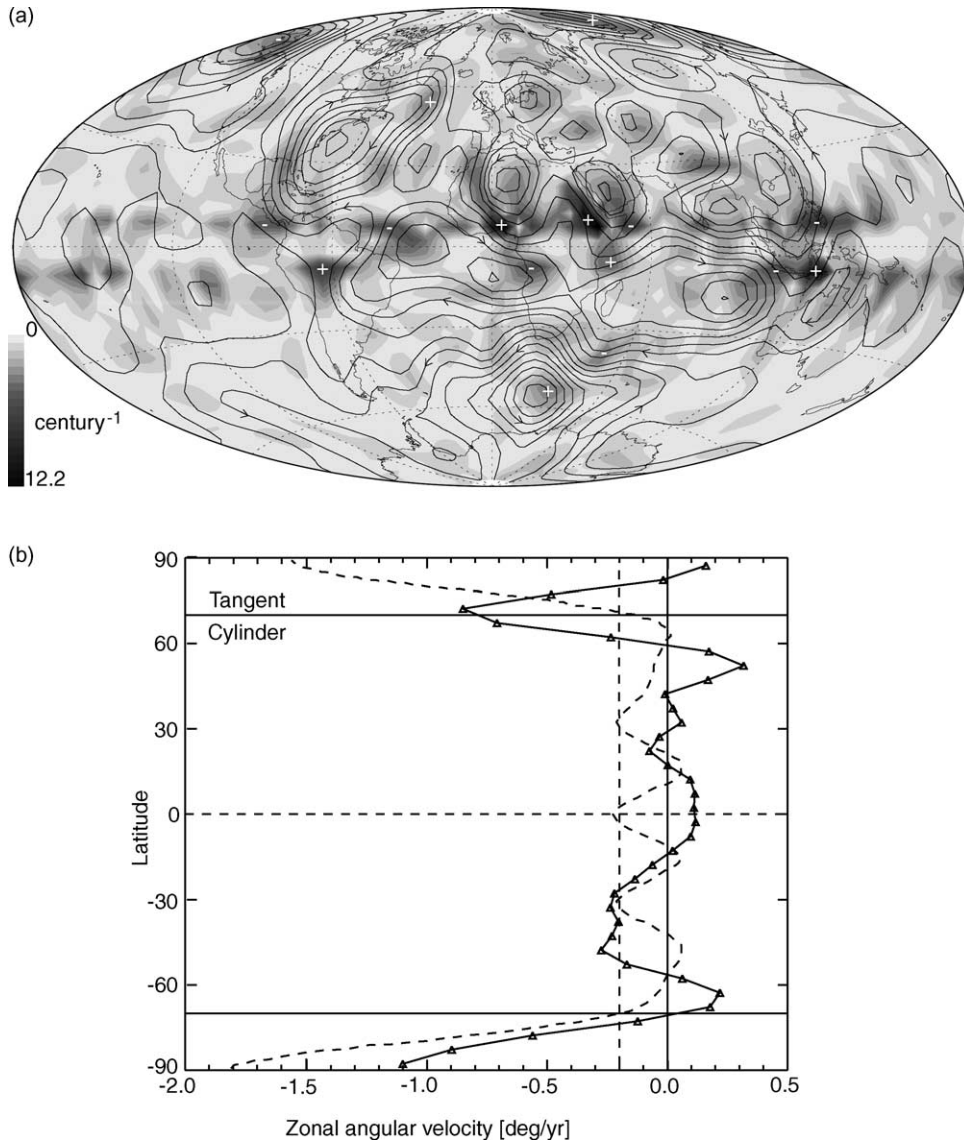| Case | Data misfit (%) | Divergence misfit (%) |
|---|---|---|
| 1 | 0.00 | 0.14 |
| 2 | 0.00 | 1.29 |
| 3 | 1.08 | 1.21 |
| 4 | 0.38 | 0.63 |
| 5 | 1.53 | 0.81 |
| 6 | 0.04 | 0.34 |

(a)



(b)



Fig. 5. Flow map (a) and zonal velocity profile (b) beneath the core-mantle boundary for the tangential geostrophy case 1 from Table 1. Contours in (a) are streamlines of the flow, grey scale represents absolute upwelling value, with + and − signs indicate upwelling and downwelling, respectively. In (b) the traditional 0.2°/year westward drift value is marked by a vertical dashed line and the zonal flow of Hulot et al. (2002) is shown by a dashed line for comparison.

hemisphere. The Atlantic hemisphere has overall higher velocities than the Pacific, and the secular variation is also higher there (see Fig. 4b). Note that the flow has a much larger length scale than does the secular variation. The solution contains a significant amount of flow along $B_r$-contours. The average ratio of the velocity component parallel to $B_r$-contours to the velocity component perpendicular to the same contours is about 1.2 (see Table 3).

The solution in Fig. 5a shows some cross-equator flow. This flow is present in this solution for two reasons. First, the tangential divergence includes the helical flow assumption as well as tangential geostrophy. Second, our grid skips the equator itself.

Table 3
Velocity ratios for different cases

| Case | $\langle \vec{v}_\parallel \rangle / \langle \vec{v}_\perp \rangle$ | $v_\theta^{\mathrm{eq}} / v_\phi^{\mathrm{eq}}$ | Sym/skew |
|------|------|------|------|
| 1 | 1.18 | 1.07 | 1.02 |
| 2 | 1.23 | 0.48 | 1.94 |
| 3 | 1.27 | 0.48 | 1.86 |
| 4 | 1.19 | 1.06 | 1.01 |
| 5 | 1.17 | 1.20 | 0.22 |
| 6 | 1.20 | 0.73 | 0.83 |

$\langle \ \rangle$ denotes the rms value over the entire grid. $\vec{v}_\parallel$ and $\vec{v}_\perp$ denote the parallel and perpendicular velocity components, respectively, with respect to the local direction of a $B_r$ contour. $v_\theta^{\mathrm{eq}}$ and $v_\phi^{\mathrm{eq}}$ denote the meridional and azimuthal flow components, respectively, averaged along the two closest latitudes to the equator. Sym/skew denotes the ratio of equatorially symmetric to antisymmetric zonal flow.

The mean equatorial meridional/azimuthal ratio is given in Table 3.

The solution contains intense vortices and jets. A clockwise vortex below Siberia coincides with an intense secular variation structure there (compare Figs. 4b and 5a). A localized jet begins beneath the Indian ocean, continues north-west beneath southern Africa and can be traced westward into the South Atlantic. This structure overlaps an intense secular variation bipolar structure aligned with the flow (again see Figs. 4b and 5a). The strongest upwellings occur near the equator, a consequence of the latitudinal dependence in the tangential geostrophy term in (39). Away from the equator, the upwellings are weaker and located at vortex centers, a consequence of the helical flow term in (39).

The zonal velocity profile for the tangential geostrophy case shown in Fig. 5b displays equal amounts of symmetry and antisymmetry with respect to the equator (see Table 3). Equatorial symmetry in the zonal velocity is consistent with a geostrophic force balance and may indicate the existence of axisymmetric columnar flow (Jault et al., 1988; Jackson et al., 1993). The zonal angular velocity in mid-latitudes of the southern hemisphere is in agreement with the traditional 0.2°/year westward drift value, but the zonal angular velocity at other latitudes is smaller and, in places, eastward. Fig. 5b includes the zonal velocity profile obtained by Hulot et al. (2002) for the same data sets. Note that our solution is less symmetric than theirs with respect to the equator. Our zonal velocity profile suggests relatively strong westward polar vortices. However, due to the small surface area of the polar cap with respect

to the data resolution, these structures are very uncertain. The existence of polar vortices was argued on the basis of numerical models (Olson and Aurnou, 1999), flow inversions (Hulot et al., 2002) and lab experiments (Aurnou et al., 2003). We find that westward polar vortices are suggested, though not well resolved in our solution. A local solution for the polar regions may shed more light on this question.

### 5.2. Sensitivity test

The geomagnetic field and the secular variation models we use are based on the Oersted and Magsat data up to spherical harmonic degree 14. In order to check the robustness of our solution with respect to small changes in the geomagnetic field model, we perform the following sensitivity test. We smooth each geomagnetic field model with a quarter cosine filter from $l_{\min} = 1$ to $l_{\max} = 13$, meaning that the $l = 1$ spherical harmonic is not filtered at all, the harmonics $l = 13$ and $l = 14$ are completely removed, and the intermediate ones are progressively filtered (see Fig. 6a and b). This type of filtering is intended to mitigate the increasing uncertainty in the secular variation power spectrum at high spherical harmonic degrees (Hulot et al., 2002). The streamfunction and zonal velocity profile of the sensitivity test using the same upwelling as in case 1 are shown in Fig. 6c and d. The solution is a smoother version of the non-truncated solution (compare Figs. 5a and 6c), with the main features present in both cases. We conclude on the basis of this test that our solution technique is robust for large flow structures, and these large structures are relatively insensitive to short wavelength errors in the secular variation model. However, using smoothed data substantially reduces smaller structures such as the polar vortices and therefore those should not be considered as very robust. The sensitivity test case contains a more equatorially-aligned flow and a more symmetric zonal flow with respect to the equator than the tangential geostrophy case 1 (see Table 3 for comparison).

### 5.3. Resolution test

We have examined the effects of grid size on our flow solutions using calculations made on a refined $2.5° \times 2.5°$ grid, again avoiding the equator and poles. The streamfunction and zonal velocity profile of this

resolution test using the same upwelling as in case 1 are shown in Fig. 7a and b. Note that the contour interval is different than the one in Fig. 5a (see details in caption of Fig. 7). The solution is much more energetic (see larger velocity values in Table 1) and contains much more small scale flow than the solution on the coarser grid (compare Figs. 5a and 7a), but the large scale circulation is similar in both cases. Two significant differences between cases 1 and 3 are worth noting. First, the flow in the resolution test case is much more aligned with equator (compare Figs. 5a and 7a, and also see Table 3). Second, the resolution test case displays more

symmetry in the zonal flow with respect to the equator than the tangential geostrophy case (compare Figs. 5b and 7b, and also see Table 3); the symmetric part of the flow in the resolution test case is about two times larger than the anti-symmetric part. Equatorial symmetry in the zonal flow is critical in the interpretation of length of day variations in terms of time dependent core flows (Jault et al., 1988; Jackson et al., 1993), and is also found in numerical dynamo simulations (Christensen et al., 1999). Fig. 7b includes the zonal velocity profile obtained by Hulot et al. (2002) for the same data sets.
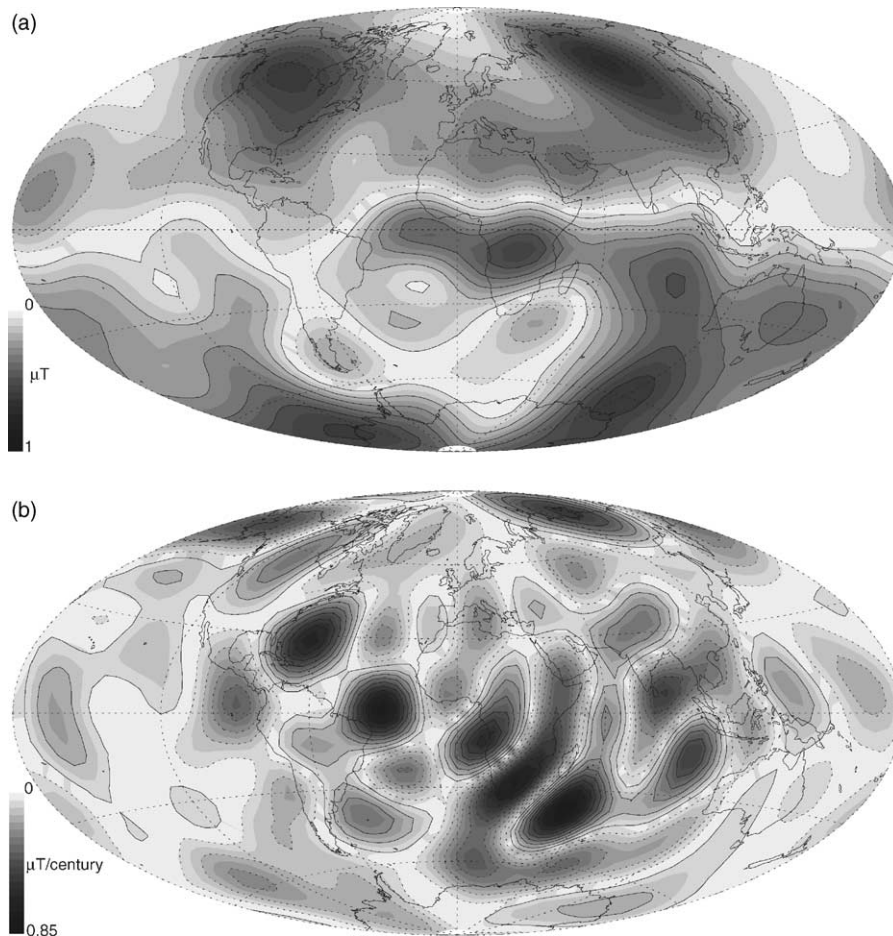


Fig. 6. Sensitivity test. Radial magnetic field (a), secular variation (b) on the core-mantle boundary, flow map (c) and zonal velocity profile (d) beneath the core-mantle boundary for low-pass filter (quarter cosine from $l_{min} = 1$ to $l_{max} = 13$) case 2 from Table 1. In (a) and (b) grey scale represents absolute values, solid lines are positive, dotted lines are negative. Note that the scale in (b) is magnified to depict the reduced secular variation with respect to the unfiltered secular variation in Fig. 4b. Contours in (c) are streamlines, grey scale represents absolute upwelling value, + and − signs indicate upwelling and downwelling, respectively. The contour interval in (c) is the same as in Fig. 5a.
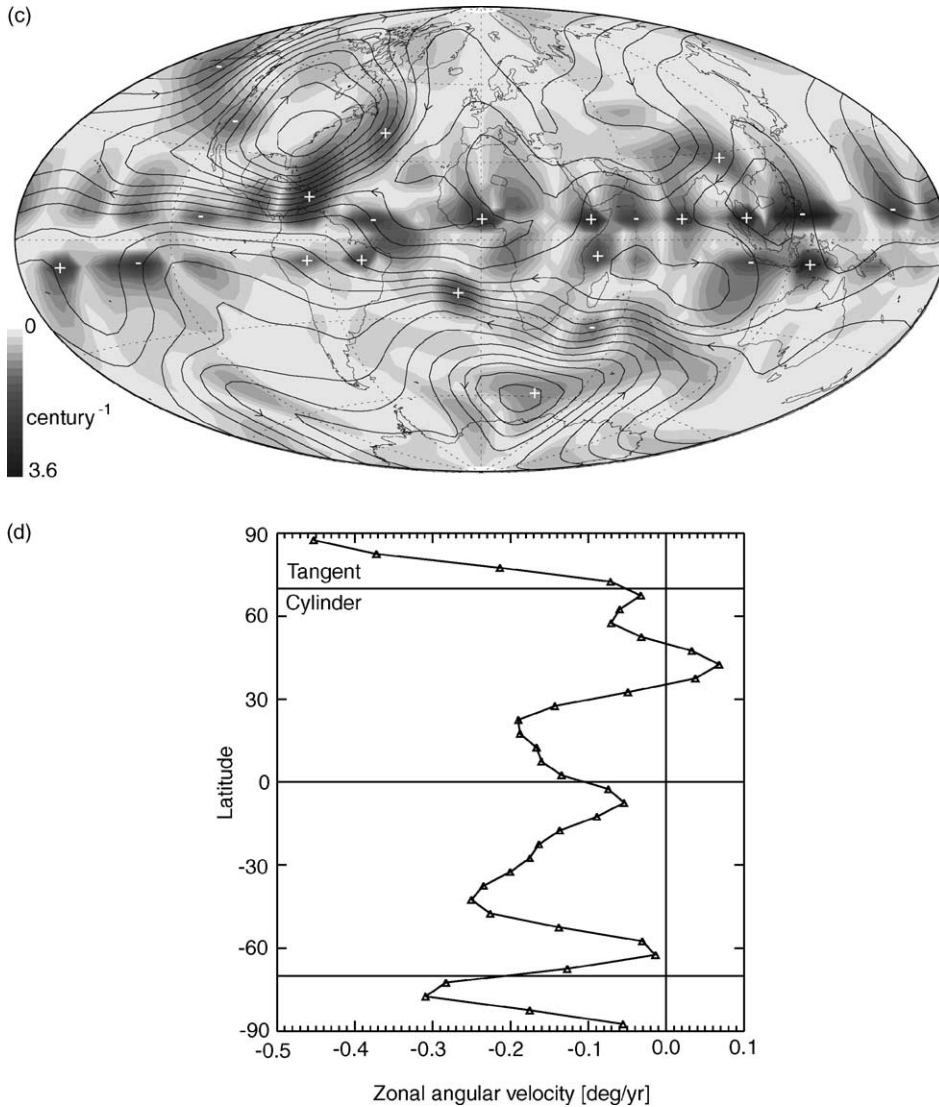
(c)



(d)



Fig. 6. (*Continued*).

## 5.4. Comparison between different physical assumptions

Fig. 8 shows the solutions for the strong helicity (case 4), weak helicity (case 5) and columnar flow (case 6) cases. Note that the contour intervals vary from one figure to another (see details in caption of Fig. 8). Most of the major features are found in the solutions for the different physical assumptions, but there are some case-to-case differences.

The toroidal flow patterns in the tangential geostrophy (case 1, Fig. 5a) and the strong helicity (case 4, Fig. 8a) are very similar. The main difference between the two cases is in the upwelling pattern. The global upwelling pattern in the strong helicity case is evenly distributed over the core-mantle boundary, whereas in the tangential geostrophy case the largest upwellings appear in the equatorial region, a consequence of the singularity of the tangential geostrophy term at the equator. To illustrate this difference, consider the
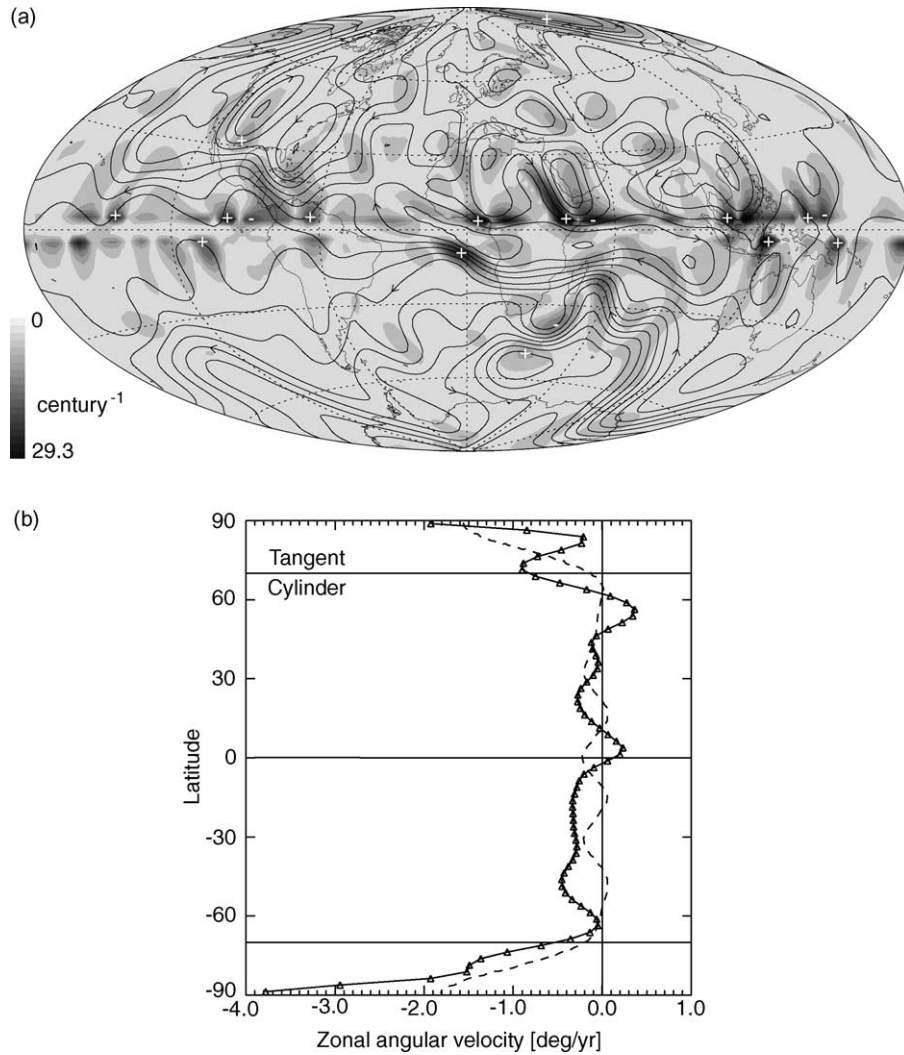
Fig. 7. Resolution test. Flow map (a) and zonal velocity profile (b) beneath the core-mantle boundary for a finer grid case 3 from Table 1. Contours in (a) are streamlines of the flow, grey scale represents absolute upwelling value, with + and − signs indicate upwelling and downwelling, respectively. The contour interval in (a) is larger by a factor of 2 than in Fig. 5a. In (b) the zonal flow of Hulot et al. (2002) is shown by a dashed line for comparison.

positive $B_r$ structure below central Africa (see Fig. 4a). This structure is stretched to the west, and as a result, a positive secular variation structure appears to its west (below the west coast of central Africa, see Fig. 4b), but no significant secular variation structure appears to its east, as would be expected from plain advection. Our solutions recover this secular variation monopole by stretching, caused by downwelling centered below the west coast of central Africa. This downwelling is

produced by a weak southward flow in the tangential geostrophy case (see Fig. 5a), or by a strong clockwise vortex in the strong helicity case (see Fig. 8a). In both cases the motion is connected to the global circulation by eastward jet along $B_r$-contours. This eastward flow produces some stretching of the magnetic field without effects of advection.

The flow pattern of the weak helicity (case 5, Fig. 8c) has elements in common with the strong helicity case,

although the velocity field of the weak helicity case is more strongly damped and has smaller velocities overall (see Table 1 for maximum and rms values).

The columnar flow solution (case 6, Fig. 8e) is also similar to the tangential geostrophy solution (case 1), with the main difference being that the columnar flow solution is more aligned with the equator. As a result, the zonal velocity in the columnar flow case has larger equatorial amplitudes (eastward at southern hemisphere, westward at northern hemisphere) than

the tangential geostrophy case (compare Figs. 8f and 5b).

The ratio of poloidal to toroidal velocities scales with the coefficient $k_0$ in the strong and weak helicity cases, and with the coefficient $c$ in the tangential geostrophy and columnar flow cases. In the strong helicity case, the secular variation can be explained by toroidal advection and stretching, whereas in other cases there is also a contribution to the secular variation from poloidal advection.
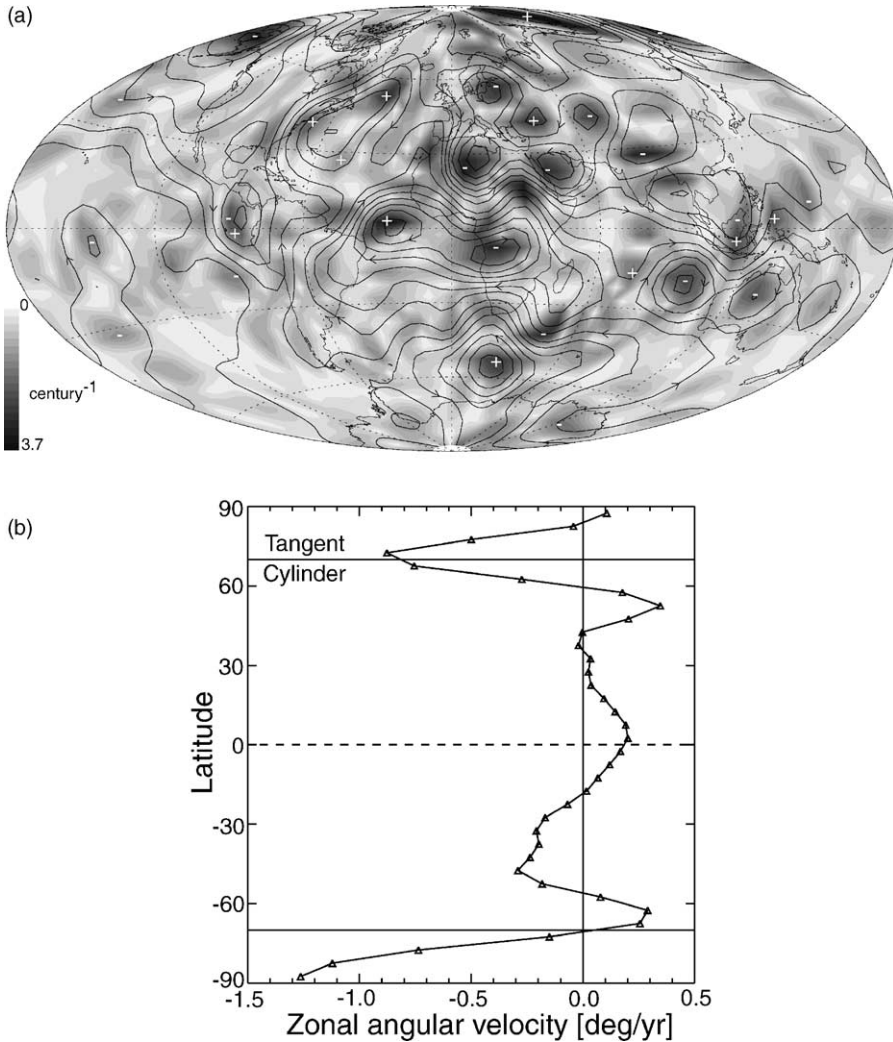


Fig. 8. Flow maps beneath the core-mantle boundary for the strong helicity (a) case 4, weak helicity (c) case 5 and columnar flow (e) case 6 (all cases from Table 1). Zonal velocity profiles for the three cases are presented at (b), (d) and (f), respectively. Contours in (a), (c) and (e) are streamlines, grey scale represents absolute upwelling value, + and − signs indicate upwelling and downwelling, respectively. The contour interval in (a) is the same as in Fig. 5a, in (c) is smaller by a factor of 1.6 than in Fig. 5a, and in (e) is larger by a factor of 1.2 than in Fig. 5a.
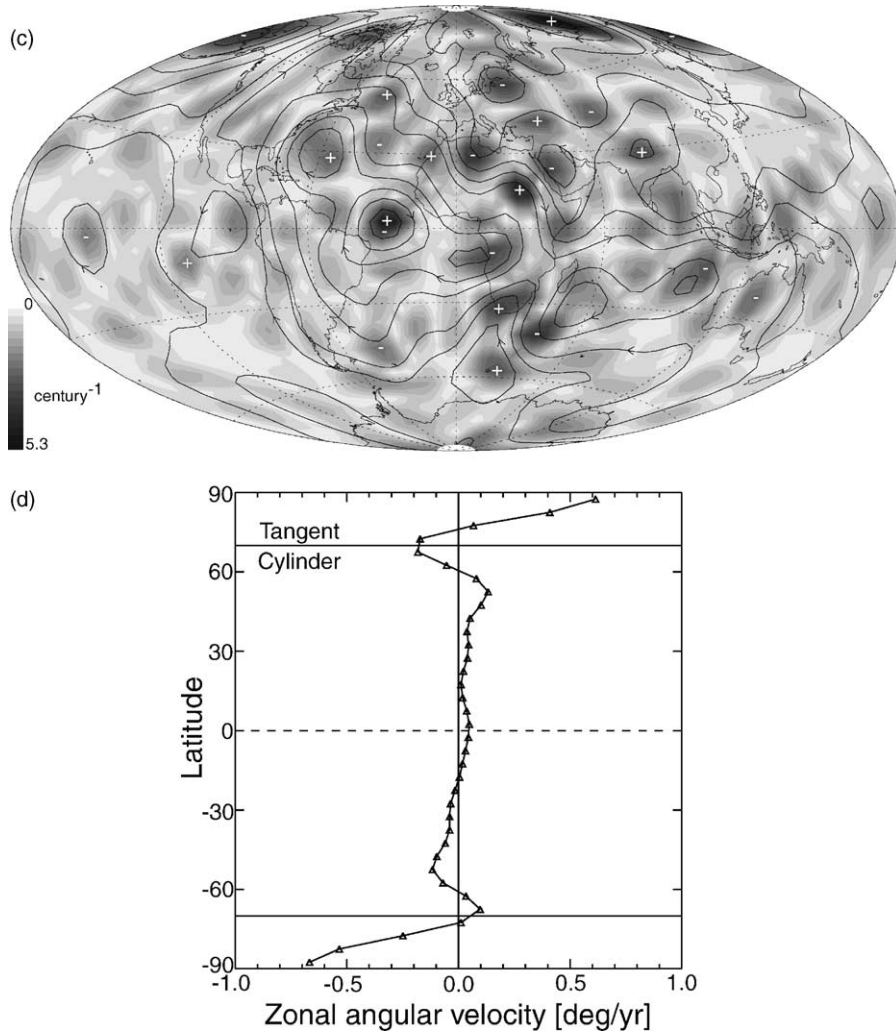
Fig. 8. (*Continued*)

The ratio of average flow component along $B_r$-contours to the average flow component perpendicular to the same contours is about 1.2 for all cases (Table 3), indicating a significant amount of such flow. Cross equatorial flow occurs least in the columnar flow case and most in the weak helicity case (again, Table 3).

Figs. 5a and 8a, c, e show little evidence of non-axisymmetric Taylor columns, i.e. vortices of opposite sign symmetric about the equator. These may be obscured by the axisymmetric flow, or, the scale of such non-axisymmetric Taylor columns of fluid might be

very small and "unseen" in the resolution of the data. Another possibility is that the Taylor columns are axisymmetric and can only be seen in the zonal angular velocity profiles (Figs. 5b and 8b, d, f), which do display some equatorial symmetry. The ratio of the symmetric zonal flow with respect to the equator to the antisymmetric one is given in Table 3. Note that the tangential geostrophy and strong helicity cases both contain about equal amounts of zonal symmetric and antisymmetric flow components with respect to the equator, whereas the zonal flow of the weak helicity case is very antisymmetric.
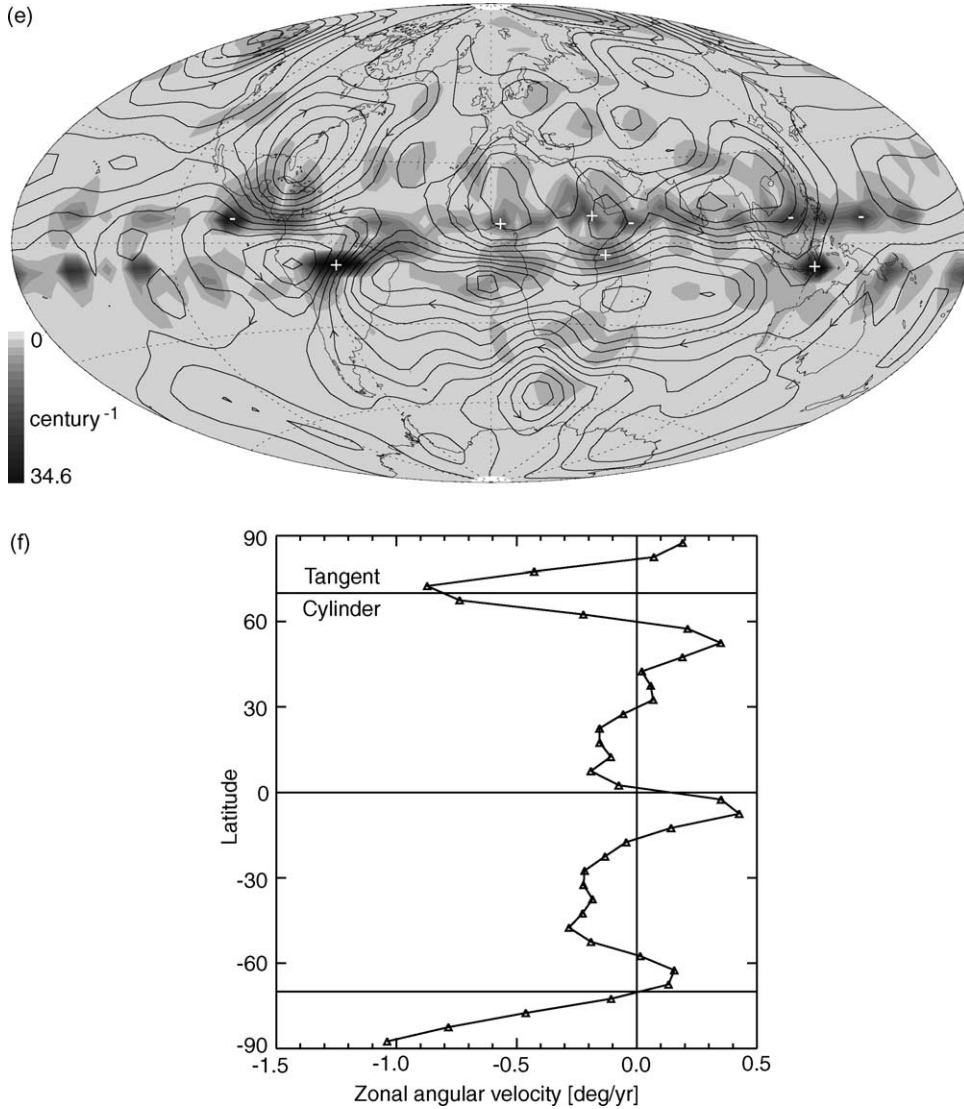
(e)



(f)



Fig. 8. (*Continued*).

## 5.5. Comparison with previous results

Here we compare the results of our tangential geostrophy case with the results obtained by Hulot et al. (2002) using the same Oersted and Magsat geomagnetic data. We further discuss some general conceptual differences between our solutions and previous ones, in terms of the differences between our method and previous spectral methods.

Our global circulation has some features in common with that obtained by Hulot et al. (2002): the Atlantic hemisphere is more active than the Pacific one, some symmetry in the zonal velocity profile with respect to the equator and similar westward drift in mid-latitudes of the southern hemisphere. However, our solution differs from the solution obtained by Hulot et al. (2002) in several features. Our average westward drift is somewhat less than theirs and our zonal flow is actually

(a)



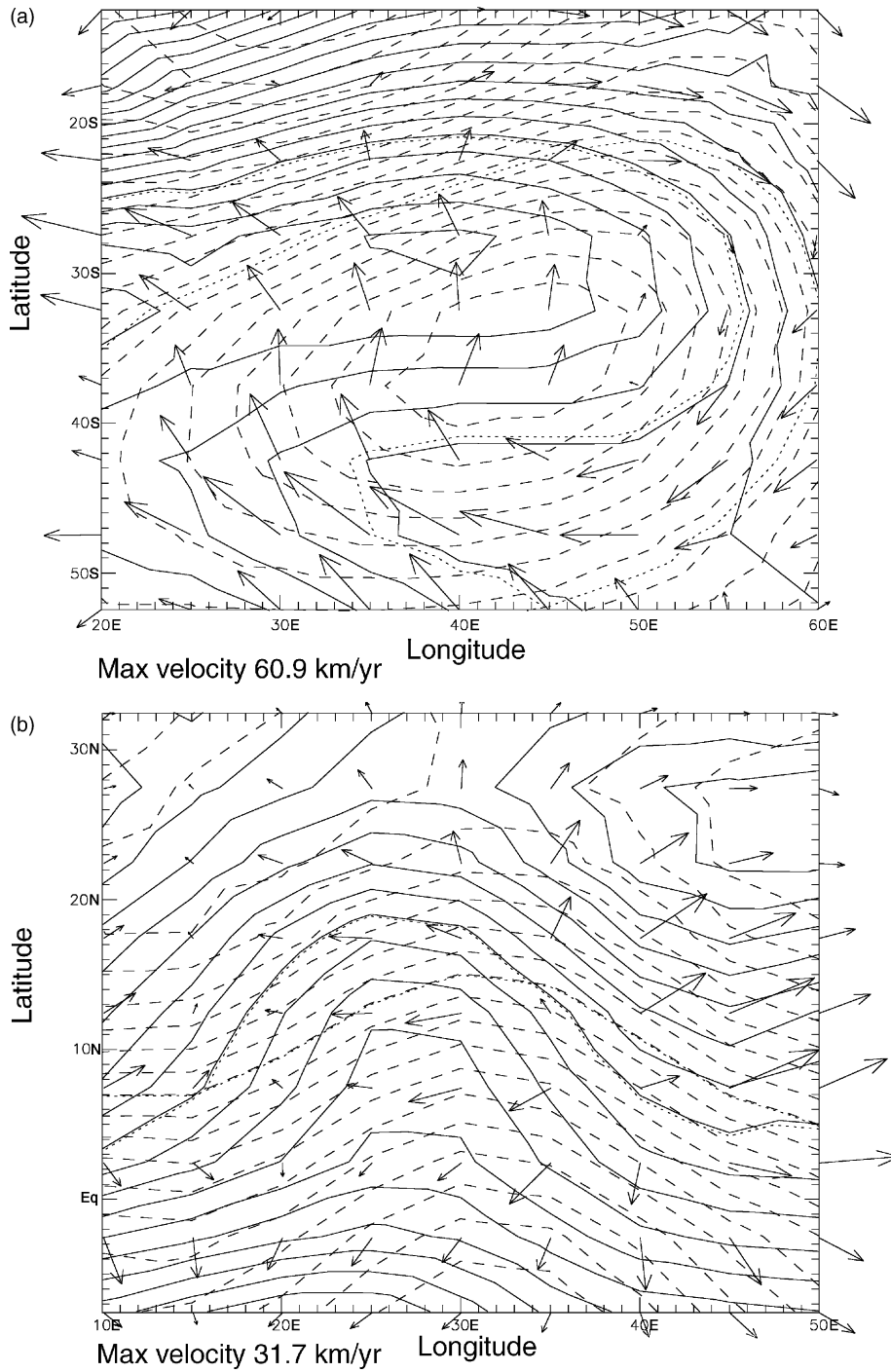Max velocity 60.9 km/yr

(b)



Max velocity 31.7 km/yr

Fig. 9. Magnetic field at 1980 (dashed lines) and 2000 (solid lines), and velocity vectors (arrows) for specific areas. $B_r = 0$ curves are shown as dotted curves in the two cases. (a) below Madagascar, showing full velocity, and (b) below Ethiopia, showing poloidal velocity.

eastward in places where theirs is westward. Also our solution contains significantly more flow along $B_r$-contours than Hulot et al. (2002).

Most previous solutions restricted the scale of their flow solution by setting some a-priori constraint on the energy spectrum. Our method does not rely on a-priori constraints; instead a solution is provided by diffusion of the streamfunction through the helical flow term. Previous spectral methods minimized "invisible flow", whereas ours allows for such flow where it is required by the helical flow assumption. In our method, the amount of flow along $B_r$-contours is specified by the amount of helicity assumed, through the value of the parameter $k_0$. Previous studies found maximal upwelling values of $\sim$2–4 century$^{-1}$ (e.g. Gire et al., 1986; Gire and LeMouël, 1990; Bloxham and Jackson, 1991). We obtain similar upwelling magnitudes in the strong and weak helicity cases, as well as in the sensitivity test case (see scales at Figs. 6c and 8a, c). However, the singularity in the tangential geostrophy term at the equator yields local stronger upwellings in the equatorial region for the tangential geostrophy case (see scale at Fig. 5a).

### 5.6. Specific areas of interest

Here we examine some specific areas of interest from the tangential geostrophy case, which show how the kinematics in our flow solution creates particular structures in the secular variation.

Fig. 9a shows the radial magnetic field on the core-mantle boundary at 1980 and 2000 and the full velocity vectors in the region below Madagascar, obtained from the tangential geostrophy case 1. Note the general consistency between the translation of the $B_r = 0$ curve and the velocity vectors. The secular variation in this area can be accounted for by simple advection of $B_r$ by toroidal velocity. The center of negative magnetic field structure shifts from (43°E, 35°S) at 1980 to (37°E, 28°S) at 2000, approximately a 9° translation to the north west in 20 years. The velocity field at this region includes a jet to the north west with maximum velocity of 68.6 km/year, which corresponds to translation of about 10° in 20 years.

Fig. 9b shows the radial magnetic field on the core-mantle boundary from the same epoch as Fig. 9a, along with the poloidal velocity vectors in the region below Ethiopia, again from case 1. In this region the contours of $B_r$ show a broad ridge structure in 1980 centered at 34°E. By 2000, this ridge structure has been translated to 28°E, and also has been sharpened. The secular variation in this area can be accounted for by stretching of magnetic field due to an upwelling. The poloidal velocity indicates the direction in which the stretching operates. Two centers of meridional velocity, which are sources of upwelling and surface divergence due to the tangential geostrophic effect, appear in the solution at (35°E, 12°N) and (0°E, 5°N). Those sources are located on both sides of the ridge structure and produce the poloidal velocities and the stretching responsible for the contraction of $B_r$ contours at this region.

## 6. Summary

We have used geomagnetic secular variation data to image the fluid flow below the core-mantle boundary by combining a previously-used assumption for the upwelling, tangential geostrophy, with a new helical flow assumption. The latter introduces streamfunction diffusion in the magnetic induction equation, and allows us to compute the fluid velocity at the top of the core using finite difference methods on a regular grid. Our method does not require any a-priori assumption about the energy or lengthscale of the flow. Our method simultaneously minimizes the secular variation data residual and guarantees that the resulted flow satisfies the physical assumption everywhere on the grid. We have used the 2000 Oersted and 1980 Magsat core geomagnetic fields. For this 20 years interval, our main findings are:

- The main flow structures common to all our up-welling models include a large anticlockwise circulation in the southern hemisphere, a clockwise vortex below Bermuda, and a westward flow over most of the southern hemisphere.
- Our solutions contain a significant amount of flow along $B_r$-contours. The ratio of the average velocity component parallel to $B_r$-contours to the average velocity component perpendicular to the same contours is about 1.2.
- The zonal average westward drift rate in mid-latitudes of the southern hemisphere is in agreement with the traditional 0.2°/year value, but the drift is smaller and even eastward at other latitudes.

- The signature of the inner core tangent cylinder is apparent in the zonal velocity profile. Polar vortices are suggested, though not well resolved in our models.
- The large scale flow in the high resolution test is qualitatively similar to the large scale flow seen with coarser resolution, but also shows some substantial differences. For example, in the higher resolution case the ratio of equatorial symmetric to antisymmetric zonal flow is about 2, whereas this ratio is about 1 with coarser resolution. This difference indicates a need for core flow models with higher spatial resolution.
- In all cases we investigated, the Atlantic hemisphere displays higher flow velocities than the Pacific.

Some of the main features of our results are similar to previous core flows obtained with the same data by Hulot et al. (2002). The results of our tangential geostrophy case contain strong mid-latitude vortices, westward drift sweeping most of the southern hemisphere, flow in the Atlantic hemisphere is more intense than in the Pacific and suggested (though not reliable) strong polar westward vortices. The flows we calculate are characterized by relatively large length scales, despite the dominance of high wavenumber structure in the secular variation. However, our solution differs from previous ones in some important aspects. Our solutions contain a significant component of flow along $B_r$-contours; this component of flow is constrained by the helical flow assumption. Hulot et al. (2002) obtained westward drift in both hemispheres, whereas our solution contains smaller and in some latitudes eastward drift.

Due to the helical flow assumption, the structure of the poloidal flow in our solutions is different from than in previous studies. Near the equator, the tangential geostrophy assumption is dominant, and poloidal flow sources are located in regions of meridional flow. However, far from the equator, the helical flow dominates, and poloidal flow sources coincide with centers of vortices.

## Acknowledgments

## Appendix A. Columnar flow upwelling

Columnar flow is defined in (19) as a horizontal translation of a column of fluid as a whole; i.e. the velocity does not vary in the direction parallel to the rotation. In a sphere, the curved boundaries do not allow for such a flow. An approximation to columnar flow in a sphere is a fluid column which is stretched/shrunk as it moves along the cylindrical $s$-direction. Assuming uniform stretching and no-flux boundary conditions, the relationship between the velocity components in cylindrical coordinates $u_s$ and $u_z$ should be linear, so that everywhere along the fluid column

$$u_z = -\frac{\eta z}{L} u_s \tag{A.1}$$

where $\eta = s/\sqrt{R^2 - s^2}$ is the slope of the spherical shell, $L = \sqrt{R^2 - s^2}$ is half the height of the column and $R$ is the sphere's radius. This assumption implies that the relative position of a particle in the fluid column is conserved. The ratio $u_z/u_s$ on the boundary equals the slope of the spherical shell to satisfy the boundary conditions, and $u_z = 0$ at the equator (symmetry). Eq. (A.1), together with the incompressible continuity equation, describe incompressible columnar flow in a sphere in cylindrical coordinates. Our goal is to express the radial upwelling term $(\partial u_r/\partial r)$ on the boundary in spherical coordinates. Using conversions between spherical and cylindrical coordinate systems

$$u_z = u_r \cos\theta - u_\theta \sin\theta \tag{A.2}$$

$$u_s = u_\theta \cos\theta + u_r \sin\theta \tag{A.3}$$

and some algebraic manipulation, (A.1) becomes,

$$u_r(\cos\theta + x\sin\theta) = u_\theta(\sin\theta - x\cos\theta) \tag{A.4}$$

where

$$x = \frac{\eta z}{L} = \frac{r^2 \sin\theta \cos\theta}{R^2 - r^2 \sin^2\theta} \tag{A.5}$$

Differentiation of (A.4) by $r$ and evaluation at $r = R$ yields the upwelling term in spherical coordinates for

a columnar flow in a sphere:

$$\frac{\partial u_r}{\partial r}(r = R) = -\frac{2\tan\theta}{R}u_\theta \qquad (A.6)$$

Using the incompressible continuity equation, the tangential divergence due to a columnar flow is

$$\nabla_h \cdot \vec{u}_h = \frac{2\tan\theta}{R}u_\theta \qquad (A.7)$$

## References

Andrews, D.G., 2000. Atmospheric Physics. Cambridge University Press, Cambridge, 229 pp.

Aurnou, J., Andreadis, S., Zhu, L., Olson, P., 2003. Experiments on convection in Earth's core tangent cylinder. Earth Planet. Sci. Lett. 212, 119–134.

Backus, G.E., 1968. Kinematics of geomagnetic secular variation in a perfectly conducting core. Philos. Trans. R. Soc. Lond. A263, 239–266.

Backus, G.E., LeMouël, J.-L., 1986. The region on the core mantle boundary where a geostrophic velocity field can be determined from frozen flux magnetic data. Geophys. J. R. Astron. Soc. 85, 617–628.

Bloxham, J., 1989. Simple models of fluid flow at the core surface derived from geomagnetic field models. Geophys. J. Int. 99, 173–182.

Bloxham, J., Jackson, A., 1991. Fluid flow near the surface of Earth's outer core. Rev. Geophys. 29, 97–120.

Busse, F.H., 1975. A model of the geodynamo. Geophys. J. R. Astron. Soc. 42, 437–459.

Chandrasekhar, S., 1961. Hydrodynamic and Hydromagnetic Stability. Dover Publications, New York, 652 pp.

Christensen, U., Olson, P., Glatzmaier, G.A., 1999. Numerical modeling of the geodynamo: a systematic parameter study. Geophys. J. Int. 138, 393–409.

Chulliat, A., Hulot, G., 2000. Local computation of the geostrophic pressure at the top of the core. Phys. Earth Planet. Int. 59, 259–287.

Cushman-Roisin, B., 1994. Introduction to Geophysical Fluid Dynamics. Prentice Hall, Englewood Cliffs, 320 pp.

Gire, C., LeMouël, J.-L., 1990. Tangentially geostrophic flow at the core-mantle boundary compatible with the observed geomagnetic secular variation: the large-scale component of the flow. Phys. Earth Planet. Inter. 59, 259–287.

Gire, C., LeMouël, J.-L., Madden, T., 1984. The recent westward drift rate of the geomagnetic field and the body drift of external layers of the core. Ann. Geophys. 2, 37–45.

Gire, C., LeMouël, J.-L., Madden, T., 1986. Motions of the core surface derived by SV data. Geophys. J. R. Astron. Soc. 84, 1–29.

Gubbins, D., 1982. Finding core motions from magnetic observations. Philos. Trans. R. Soc. Lond., Ser. A 306, 249–256.

Hulot, G., Eymin, C., Langlais, B., Mandea, M., Olsen, N., 2002. Small-scale structure of the geodynamo inferred from Oersted and Magsat satellite data. Nature 416, 620–623.

Jackson, A., Bloxham, J., Gubbins, D., 1993. Time-dependent flow at the core surface and conservation of angular momentum in the coupled core-mantle system. In: LeMouël, J.-L., Smylie, D.E., Herring, T. (Eds.), Dynamics of Earth's Deep Interior and Earth Rotation, Geophysical Monograph 72 IUGG, vol. 12, pp. 97–107.

Jault, D., Gire, C., LeMouël, J.-L., 1988. Westward drift, core motions and exchanges of angular momentum between core and mantle. Nature 333, 353–356.

Kundu, P.K., 1990. Fluid Mechanics. Academic Press, San Diego, 638 pp.

LeMouël, J.-L., 1984. Outer core geostrophic flow and secular variation of Earth's magnetic field. Nature 311, 734–735.

Lilly, D.K., 1986. The structure, energetics and propagation of rotating convective storms. Part 2: helicity and storm stabilization. J. Atmos. Sci. 43, 126–140.

Olson, P., Aurnou, J., 1999. A polar vortex in the Earth's core. Nature 402, 170–173.

Olson, P., Christensen, U., Glatzmaier, G.A., 1999. Numerical modeling of the geodynamo: mechanisms of field generation and equilibration. J. Geophys. Res. 104, 10383–10404.

Olson, P., Sumita, I., Aurnou, J., 2002. Diffusive magnetic images of upwelling patterns in the core. J. Geophys. Res. 107, doi:10.1029/2001jb000384.

Pais, A., Hulot, G., 2000. Length of day decade variations, torsional oscillations and inner core superrotation: evidence from recovered core surface zonal flows. Phys. Earth Planet. Inter. 118, 291–316.

Protter, M.H., Weinberger, H.F., 1967. Maximum Principles in Differential Equations. Prentice Hall, Englewood Cliffs, 261 pp.

Rau, S., Christensen, U., Jackson, A., Wicht, J., 2000. Core flow inversion tested with numerical dynamo models. Geophys. J. Int. 141, 485–497.

Salmon, R., 1998. Geophysical Fluid Dynamics. Oxford University Press, New York, 378 pp.

Sardeshmukh, P.D., Hoskins, B.J., 1987. On the derivation of the divergent flow from the rotational flow: the χ problem. Q. J. R. Meteorol. Soc. 113, 339–360.

Sardeshmukh, P.D., Hoskins, B.J., 1988. The generation of global rotational flow by steady idealized tropical divergence. J. Atmos. Sci. 45, 1228–1251.

Sverdrup, H.U., 1947. Wind-driven currents in a baroclinic ocean, with application to the equatorial currents of the eastern Pacific. Proc. Natl. Acad. Sci. 33, 318–326.

Voorhies, C.V., 1986. Steady flows at the top of Earth's core derived from geomagnetic field models. J. Geophys. Res. 91, 12,444–12,466.

Whaler, K.A., 1980. Does the whole of Earth's core convect? Nature 287, 528–530.

Whaler, K.A., 1986. Geomagnetic evidence for fluid upwelling at the core-mantle boundary. Geophys. J. R. Astron. Soc. 86, 563–588.

Zatman, S., Bloxham, J., 1997. Torsional oscillations and the magnetic field within the Earth's core. Nature 388, 760–763.